Structure-function-dynamics relationships in the peculiar *Planktothrix* PCC7805 OCP1: impact of his-tagging and carotenoid type.

Adjélé Wilson[1§], Elena A. Andreeva[2,3§], Stanislaw J. Nizinski[4,5§], Léa Talbot[1], Elisabeth Hartmann[3], Ilme Schlichting[3], Gotard Burdzinski[5], Michel Sliwa[4*], Diana Kirilovsky[1*] and Jacques-Philippe Colletier[2*]

[1] Université Paris-Saclay, CEA, CNRS, Institute for Integrative Biology of the Cell (I2BC), 91198 Gif-sur-Yvette, France.

[2] Univ. Grenoble Alpes, CEA, CNRS, Institut de Biologie Structurale, 38000 Grenoble, France.

[3] Max-Planck-Institut für medizinische Forschung, Jahnstrasse 29, 69120 Heidelberg, Germany.

[4] Univ. Lille, CNRS, UMR 8516, LASIRE, LAboratoire de Spectroscopie pour les Interactions, la Réactivité et l'Environnement, Lille 59000, France

[5] Quantum Electronics Laboratory, Faculty of Physics, Adam Mickiewicz University in Poznań, Uniwersytetu Poznańskiego 2, Poznan 61-614, Poland

[§] These authors contributed equally to this work.
* Correspondence to: J.-P. Colletier (colletier@ibs.fr), D. Kirilovsky (diana.kirilovsky@cea.fr); M. Sliwa (michel.sliwa@univ-lille.fr)

Keywords: cyanobacteria – flash photolysis – photosynthetic pigments – structure function relationships – X-ray diffraction

Highlights:

- Complete functional characterization of *Synechocystis* and *Planktothrix* OCPs
- Hitherto unknown structures of ECN- and CAN-functionalized *Planktothrix* OCP
- Insights into fs-s timescale photodynamics of ECN- and CAN-functionalized *Synechocystis* and *Planktothrix* OCPs

Abstract

The orange carotenoid protein (OCP) is a photoactive protein involved in cyanobacterial photoprotection. Here, we report on the functional, spectral and structural characteristics of the peculiar *Planktothrix* PCC7805 OCP (Plankto-OCP). We show that this OCP variant is characterized by higher photoactivation and recovery rates, and a stronger energy-quenching activity, compared to other OCPs studied thus far. We characterize the effect of the functionalizing carotenoid and of his-tagging on these reactions, and the time scales on which these modifications affect photoactivation. The presence of a His-tag at the C-terminus has a large influence on photoactivation, thermal recovery and PBS-fluorescence quenching, and likewise for the nature of the carotenoid that additionally affects the yield and characteristics of excited states and the ns-s dynamics of photoactivated OCP. By solving the structures of Plankto-OCP in the ECN- and CAN-functionalized states, each in two closely-related crystal forms, we further unveil the molecular breathing motions that animate Plankto-OCP at the monomer and dimer levels. We finally discuss the structural changes that could explain the peculiar properties of Plankto-OCP.

Introduction

Photosynthetic organisms have evolved to make use of nearly all photons absorbed by their light-harvesting antennas. Under light stress conditions, however, the photosynthetic electron transport chain becomes saturated leading to the formation of harmful reactive oxygen species (ROS), e.g., singlet oxygen ($^1O_2$) [1, 2], that can damage the photosystems and other cellular machineries, eventually leading to cell death. Accordingly, photosynthetic organisms have developed a variety of mechanisms, altogether referred-to as non-photochemical quenching (NPQ), that are aimed at reducing the amount of energy reaching the photochemical reactions centers thereby avoiding accumulation of ROS [3]. In a vast majority of cyanobacterial strains, the main light-harvesting antenna is a large soluble complex, the phycobilisome (PBS), and the soluble 35 kDa photoactive Orange Carotenoid Protein (OCP) is at the center of the NPQ mechanism (for review: [4-6]). OCP is capable both of dissipating the excess energy harvested by the PBS [7], and of quenching the produced harmful singlet-oxygen [8, 9]. For the energy quenching mechanism to be elicited, OCP must be photoactivated, which triggers the changes in protein structure and pigment position required for PBS binding and discharge of its excessive energy [10, 11]. Specifically, upon absorption of a blue-green photon, OCP converts from an inactive dark-adapted state (denoted as OCP^O, due to its orange color) into an active light-adapted state (denoted OCP^R, due to its red color). OCP^O is characterized by two absorption maxima at 475 and 495 nm (vibronic structure), while OCP^R displays a single broader absorption peak between 510 and 530 nm [11]. The photoactivation quantum yield of the protein is notoriously low, viz. 0.2 % [12], meaning that the OCP-supported photoprotective mechanism is at play only under high light conditions and that the concentration of OCP^R is null, or very low, in darkness and under low light conditions [11, 13]. Phylogenic studies of OCP sequences allowed their classification into three distinct clades, viz. OCP1, OCP2 and OCPX [14]. Members of the OCP1 clade are characterized by a slow OCP^R to OCP^O thermal recovery (at 8°C) that is accelerated by the presence of the fluorescence recovery protein (FRP), whereas OCP2 and OCPX exhibit a faster thermal recovery (even at 8°C) that is not affected by the presence of FRP [15, 16].

The best characterized OCPs are OCP1s from *Arthrospira maxima* and *Synechocystis* PCC 6803, hereafter referred to as *Arthrospira* and *Synechocystis* OCP, respectively. For both, the dark-adapted structure was solved [8, 17], which revealed a conserved two-domain modular architecture. The fully α-helical N-terminal domain (NTD, residues 1-165), unique to cyanobacteria, and the C-terminal domain (CTD, residues 187-320), structurally belonging to the nuclear transport factor-2 superfamily (NTF2), encase at their interface a ketocarotenoid pigment, e.g. 3'-hydroxyechineone (3'-hECN) [8, 17]. Notwithstanding the presence of a linker that covalently attaches the NTD and CTD, the dark-adapted state is stabilized by two main

3

protein interfaces, viz. (i) the central interdomain interface, which features two highly-conserved H-bond (N104-W277) and salt-bridge (R155-E244); and (ii) the interface between the N-terminal helix (also coined, N-terminal extension or NTE) and the CTD β-sheet [8], which features six to seven H-bonds depending on species. Additionally, the ketocarotenoid pigment buries ≈ 95% of its highly hydrophobic surface into the binding tunnel spanning the two domains, and therefore also contributes to the stabilization of the OCP^O, with a buried surface area (BSA) of 786 Å^2 and a surface complementarity of ~83%. The sole polar interactions between the ketocarotenoid and the protein scaffold are the H-bonds established between the carbonyl oxygen of its β1 ring and the side chain hydroxyl and amine of CTD residues Y201 and W288 (*Synechocystis* OCP residue numbering), respectively [8, 17] . Rupture of these H-bonds is the first event along a photo-activation cascade that involves several 'red' intermediate states spanning the ps to second time scale [12, 18-20] and culminates with dissociation of the two domains following the 12 Å translocation of the carotenoid into the NTD [21]. Dissociation of the two domains is essential for the energy-quenching function, as only OCP^R is capable of binding to the PBS [10, 11]. This activity is measured as the quenching of PBS fluorescence, itself induced by exposure to blue-light.

Despite the considerable knowledge acquired on OCP in the last decades, the photoactivation mechanism is still under debate. Notably, the very first instants of the photoactivation mechanism remains elusive. Numerous computational and time-resolved spectroscopic studies have recently sought to shed light on the structure, formation and decay of the carotenoid excited states associated with OCP photoactivation ([19, 22-24]; Figure 1). Notably, it was demonstrated that upon photoexcitation, three ps-lived intermediate states are formed following the sub-ps decay of the initial S_2 state, viz. an S_1 and an intra-molecular charge transfer (ICT) excited states [25, 26], and an S* state [19] that was initially proposed to correspond to a vibrationally hot S_0 population [27]. Recently, however, it was proposed that the S* state, characterized by a longer lifetime than the S_1 and ICT states [19, 28], is also an excited state which serves as the precursor of the first photoproduct, P_1, in which the H-bonds between the carotenoid and the protein are broken and the protein is (therefore) already 'red' (difference absorption spectrum peaking at 565 nm) [19]. The debate however remains open concerning the nature of the S* state [29-31] and its putative role as the precursor of P_1. Indeed, recent results from our laboratories show that while the photoactivation speed of OCP^R is independent of irradiation light (470 nm versus 540 nm), the concentration of S* decreases by ≈ 30% when 540 nm light is used to trigger photoactivation (Nizinski et al., submitted; doi.org/10.1101/2021.12.26.474187). Hence, S* cannot be the sole precursor of P_1. Evolution of this state (50 ns lifetime), wherein the carotenoid is likely untethered from its CTD H-bonding partners, leads to a repositioning of the carotenoid in the tunnel, in close vicinity of the dark-

state position (P_2; 0.5 – 1 µs) [19]. After a first partial movement into the NTD (P2'; 10 µs) [19], the ketocarotenoid completes its translocation into the NTD, reaching the position it occupies in the final OCP^R in around 10 µs (P_3);[19, 23]. Conformational changes in the NTE and CTT ensue (P_M and P_X ~10 ms and 35 ms), followed by an opening of the protein upon dissociation of the two domains (~100 ms) [23]. Thus, the formation of the photoactive OCP^R is a multi-step reaction spanning at least fourteen decades in times [12, 19, 23]. All steps, excluding the $P_{2'}$ to P_3 and P_3 to P_M transitions, are accompanied by recovery to the initial OCP^O state, explaining the low quantum yield. About 1 and 0.2 % of molecules reach the P_1 state [19] and the final OCP^R state [12, 19, 23] (Nizinski et al., submitted; doi.org/10.1101/2021.12.26.474187) (Figure 1), respectively.
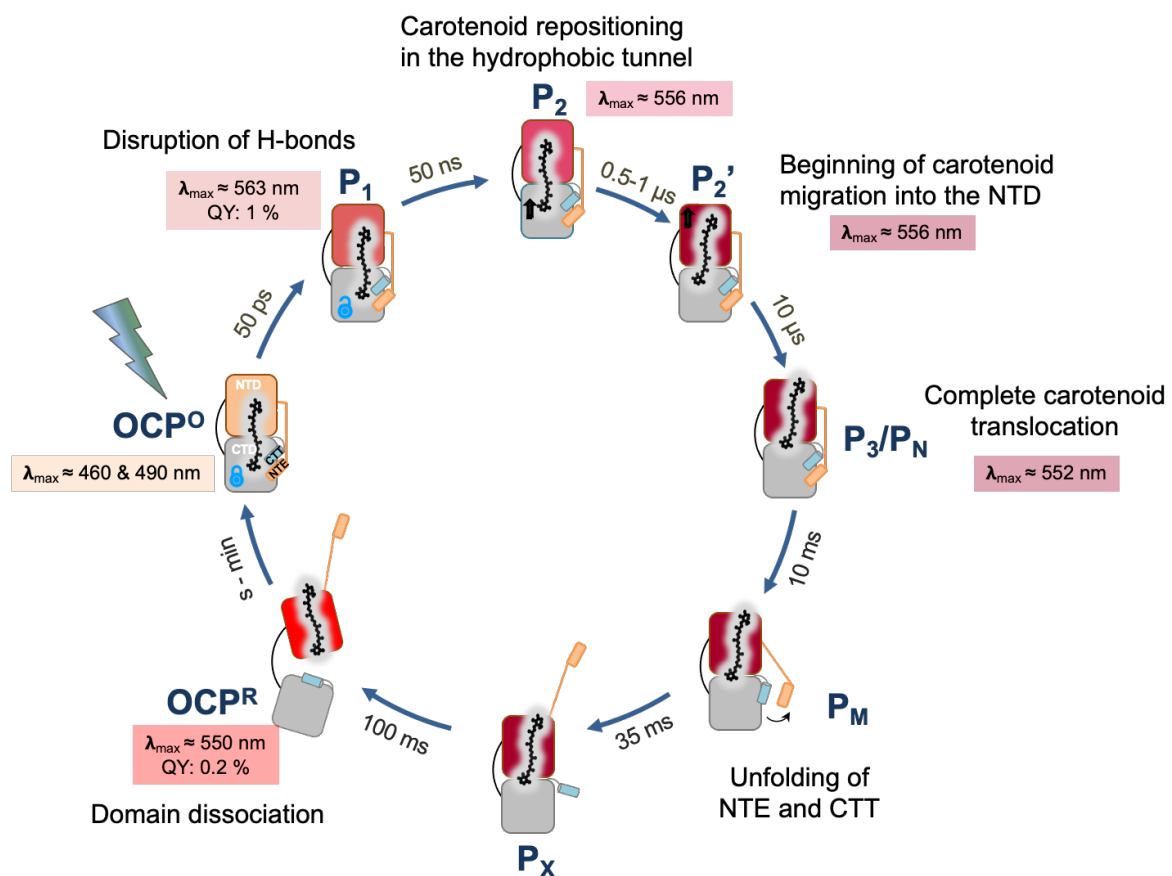

Figure 1: Formation of OCP^R is a multi-step reaction that spans 12 decades in time. The figure which presents a working model for OCP photoactivation, summarizes findings from multiple studies [12, 19, 23]. The wavelength of maximum difference-absorbance (after subtraction of the OCP^O signal) is indicated for all intermediate states characterized to date. The P_1, P_2, $P_{2'}$ and P_3 were observed by Konold et al. 2019 in transient absorption UV-Vis experiments upon excitation at 470 nm of Ntag-Syn-OCP_{ECN} [19]. Of important note, $P_{2'}$ was only observed in transient IR experiments, suggesting that it is characterized by a conformational change in the protein scaffold that does not influence the carotenoid electronic properties. P_N/P_M and P_X were observed by Maksimov et al. in time-resolved fluorimetry experiments upon excitation at 262 nm of the ECN-functionalized OCP-3FH mutant (W41F, W101F, W110F and W277H) featuring a single tryptophan at position W288 [23].

In all recent studies on OCP, the protein was expressed recombinantly [32] and to accelerate purification, a six-histidine tag (6XHis-tag) was introduced at the N-terminus (OCP produced in *E. coli* cells) or C- terminus (OCP produced in *Synechocystis* and *E. coli* cells). However, it was shown that after migration of the carotenoid from the NTD/CTD interface into the NTD (≈ 0.5 µs) formation of OCP^R requires, prior to domain separation, the detachment of the N-terminal helix αA (or NTE) from the CTD β-sheet [19, 33, 34]. Likewise, the C-terminal helix αN (or CTT) was proposed to reposition upon domain separation – possibly to "clog" the otherwise-exposed highly-hydrophobic CTD-half of the carotenoid tunnel [34-36]. Hence, presence of a His-tag at either the N- or C-terminal extremity of the protein can influence the kinetics of photoactivation and thermal recovery, respectively. In support of this hypothesis, we recently reported the finding that His-tag position affects: i) the photoactivation efficiency, with OCP^R accumulation being slower when the His-tag is present at the C-terminus (C-tagged OCP); ii) the lifetime of excited states, with those being shorter for C-tagged OCP); and iii) the spectral signatures of S_1 and S* states. However, the position of the tag does not influence P1 formation quantum yield (QY) suggesting that the more efficient photoactivation of the N-tagged protein is related to molecular events occurring on the nano- to millisecond timescales (Nizinski et al., under revision). Regardless, it also remains unclear whether or not presence of the His-tag has an influence on PBS energy quenching and on thermal recovery. Also lacking is a thorough structure-function-dynamics comparison between OCP from various strains to understand how subtle changes in the structure may affect the function, its regulation or both. For example, it was recently reported that despite a lower intracellular OCP concentration and a quasi-strict conservation of the amino acids lining the OCP carotenoid tunnel, the amplitude of the OCP-related PBS-fluorescence quenching is larger in the cyanobacterium *Planktothrix* PCC 7805 than in *Synechocystis* PCC 6803 [37], and likewise for the PBS-fluorescence recovery. Hence, the *Planktothrix* OCP may differ in structure and/or structural dynamics from the other OCPs described to date.

Finally, it has been shown that while the naturally-occurring pigment in *Synechocystis* and *Arthrospira* OCP is 3'-hydroxyechinenone (3'-hECN), the protein may also be functionalized by other similarly-length ketocarotenoids, the palette of which will depend on species. Indeed, upon knock-out of the gene coding for the hydrolase converting ECN into hECN, *Synechocystis* OCP binds ECN [38], and likewise when the protein is overexpressed in *Synechocystis* cells, due to the low amount of hECN (≈ 1% of all ketocarotenoids) [11, 39]. When expressed recombinantly in *E. coli* cells [32], *Synechocystis* OCP can be complexed with ECN, canthaxanthin (CAN) or zeaxanthin (ZEA), depending on the set of carotenoid-producing genes that are co-transformed with the gene coding for the OCP. This feature holds true for all OCP variants produced recombinantly in carotenoid-producing *E. coli* cells, including OCP1

from *Synechocystis*, *Arthrospira* and *Tolypothrix* [15, 32], OCP2 from *Tolypothrix* and *Synechocystis* 7508 [15, 16], and OCPX from *Scytonema* and *Synechocystis* 7508 [16]. To date, only *Tolypothrix* OCP was found to bind canthaxanthin (CAN) when overexpressed in *Tolypothrix* cells [30]. Early studies showed that the relative populations of the carotenoid S_1 and ICT excited-states depend on the carotenoid that functionalizes OCP, with virtually no ICT in *Synechocystis* OCP functionalized with the fully symmetric CAN, but up to 50% ICT in OCP functionalized with the non-symmetric ECN [30, 40]. It was then proposed that the absence of the ICT state is a consequence of the fully symmetric nature of the CAN pigment, which is absent in ECN [30, 40]. However, the P_1 state was not identified at the time, so that it remains elusive whether or not the change in functionalizing carotenoid also affects the yield of this presumed photoproductive intermediate. Moreover, it is unknown if the rate of OCP^R accumulation and recovery as well as the yield of intermediary photoproducts are influenced by the nature of the functionalizing carotenoid.

Here, we address these gaps in knowledge by performing a comparative structure-function study on the OCP1 from two different strains, viz. *Synechocystis* PCC 6803 (Syn-OCP), and *Planktothrix* PCC 7805 (Plankto-OCP). For both OCP1 variants, the kinetics of photoactivation, thermal recovery and PBS-fluorescence quenching were assessed in the native (non-tagged), N-tagged and C-tagged states, and with ECN or CAN as the functionalizing carotenoid. We observe that the presence of the His-tag at the C-terminus has a larger influence on photoactivation, thermal recovery and PBS-fluorescence quenching than its presence on the N-terminus. We found that the nature of the carotenoid influences the yield and characteristics of excited states, the ns-s dynamics of photoactivated OCP and the thermal recovery, leading to different rates of OCP^R accumulation, and of PBS-fluorescence quenching. As only the structures of ECN- and CAN-functionalized Syn-OCP [17, 21] were available, we solved the Plankto-OCP structures in both the ECN- and CAN-functionalized states. At 1.4 – 1.8 Å resolution, our structures shed light on the molecular breathing motions that animate Plankto-OCP monomers and dimers, and point to subtle changes outside of the carotenoid tunnel explaining the peculiar properties of Plankto-OCP.

Materials and Methods

Construction of plasmids for *ocp* gene expression in *E. coli* cells.

The plasmids pCDF-OCPSynCtag (coding for C-tagged Syn-OCP), pCDF-NtagOCPSyn (coding for N-tagged Syn-OCP) featuring the *Synechocystis ocp* gene were described in [32]. To construct the plasmid *pCDF*-OCPSyn, and thereafter express the native (non-tagged) *Synechocystis ocp* (*srl963*) gene in *E. coli* cells, the nucleotides coding for the N-terminal his-tag in the plasmid pCDF-NtagOCPSyn were excised by mutagenesis using F-ocpSynNative: 5'-ATAAGGAGATATACCATGCCATTCACCATTGACTCT-3' and R-Duet: 5'-CATGGTATATCTCCTTATTAAAGTTAAACAAAATTA-3' primers in order to create the plasmid *pCDF*-OCPSyn.

To construct the plasmid containing the *Planktothrix agardhii* PCC *7805 ocp* (*PLAM_2315*) gene, a PCR using genomic DNA of *Planktothrix agardhii str. 7805* as template and forward (F-OCPPlank EcoR1: 5'-CGATGCGAATTCTTCATTTACAGTCGATTCAGCCC-3') and reverse (R-OCPPlank Not1: 5'-CATTATGCGGCCGCCTTCCCCCTTAAATCACAAG-3') primers was performed. Then, the PCR products were cloned in pCDFDuet-1 previously digested by EcoRI and NotI which includes the nucleotides encoding for 6x His-terminal tag. This plasmid, named pCDF-NtagOCPPx, was thereafter used to express *Planktothrix* OCP his-tagged at the N-terminus.

To synthesize *Planktothrix* OCPs without tags, the nucleotides coding the 6x His-tag in the pCDF-NtagOCPPx plasmid were suppressed using F-OCPPxNoTag: 5'-TTAATAAGGAGATATACCATGTCATTTACAGTCGATTCAGCCCGTGGG-3' and R-Duet (see above) to create the plasmid pCDF-OCPPx and express the native (non-tagged) *Planktothrix* OCP. Then, a nucleotide sequence encoding 6 histidine residues was added at the 3'end by mutagenesis using the plasmid pCDF-OCPPx without tag as template and synthetic primers (F-DuetOCPPx Ctag: 5'-CACCACCACCACCACCACTAATTAATAAACGAATCTAATTTGATATAGC-3' and R-DuetOCPPx Ctag: 5'-GTGGTGGTGGTGGTGGTGACGAACTAAATTTAACAACTCTTTAGGTG-3'). Thereby, we obtained the plasmid pCDF-CtagOCPPx which was used to express *Planktothrix* OCP his-tagged at the C-terminus.

Construction of plasmids for *frp* gene expression in *E. coli* cells.

The plasmid used to express the *Synechocystis frp* gene in *E. coli* was described in [10]. To express the *Planktothrix agardhii* PCC *7805 frp* (*PLAM_2314*) gene in *E. coli*, the *frp* gene was amplified by PCR using forward (F-FRPPlank EcoR1: 5'-CGATGCGAATTCTCAAGTAAATGAGATTGAATG-3') and reverse (R-FRPPlank Not1: 5'-

TGCTTAGCGGCCGCAACTCAAATTGTTTTAAGAATCCCCG-3') primers. The resulting fragment was cloned between the EcoRI and NotI sites of the pCDFDuet-1 plasmid which contains the nucleotides encoding for 6x His-tag.

Holo-OCPs production, Isolation and Purification

The production and isolation of holo-OCPs were previously described [32]. FRP isolation was described in [10]. To isolate OCPs without tag, *E. coli* cells were resuspended in lysis buffer (40 mM Tris-HCl pH 8, 1 mM EDTA, 1 mM PMSF, 1 mM caproic acid, 1 mM benzamidic acid, 50 µg mL^{-1} DNAse) and broken using a French Press. Membranes were pelleted and the supernatant was loaded on a Whatman DE-52 cellulose column. The OCP was eluted using a gradient of 60-80 mM NaCl in 40 mM Tris-HCl pH 8. A second purification step was performed by hydrophobic interaction chromatography (HiTrap Phenyl HP column, GE Healthcare) and the OCP was eluted in 40 mM Tris-HCl pH 8, 0.5M NaCl. The eluate was dialyzed overnight against 40 mM Tris-HCl pH 8 at 4°C (2 Liters).

Absorbance measurements and kinetic analysis.

Absorbance spectra of PBS and OCPs and kinetics of OCP photoactivation (illumination with 5 000 µmol photons.m-^{2}. s^{-1} of white light), and dark recovery were measured with a Specord S600 spectrophotometer (Analytic Jena) using 1 cm path-length cuvette. Experiments were performed at an OCP concentration of ~4.8 µM, corresponding to an OD of 0.3 at 496 nm (calculated using an epsilon equal to 63 000 M^{-1}.cm^{-1} [41]). Spectra were acquired in the 250–700 nm range for each time point. OCP^O photoactivation and OCP^R recovery were both monitored by measuring the changes of absorbance at 550 nm.

Isolation of PBS and fluorescence measurements.

The purification of PBS from *Synechocystis* PCC 6803 and *Planktothrix agardhii* PCC 7805 was performed as previously described [42]. The PBS-fluorescence quenching yield was monitored using a pulse amplitude-modulated fluorimeter (101/102/103-PAM, Walz). Measurements were made in a 1 cm path-length stirred cuvette. PBS quenching induced by holo-OCPs was measured in 0.5 potassium phosphate buffer (pH 7.5) at 23 °C under strong blue–green light (900 µmol photons m^{-2} s^{-1}). The PBS concentration used was 0.012 µM and the ratio of OCP to PBS was 40:1. OCP samples were pre-illuminated with 5 000 µmol photons m^{-2} s^{-1} of white light at 4°C. Samples in Pasteur pipettes were quickly frozen by immersion in liquid nitrogen. Fluorescence emission spectra at 77K were recorded using a CARY Eclipse fluorescence spectrophotometer fluorometer (Varian).

Protein Separation

Proteins were analyzed by SDS-PAGE on 15% polyacrylamide gels in a Tris-MES buffer [43]. PBS samples were concentrated by precipitation with 10% (v/v) TCA prior to loading (equal protein quantities in each lane). 10 µL at a PBS concentration of 0.5 µM were deposited per well. The gels were stained by Coomassie Brilliant Blue.

Femtosecond transient absorption spectroscopy (0 – 1 ns timescale)

Transient absorption measurements were performed using a Helios system from Ultrafast Systems. A short-pulse titanium sapphire oscillator (Mai Tai, Spectra Physics, 70 fs pulse length) followed by a high-energy titanium sapphire regenerative amplifier (Spitfire Ace, Spectra Physics, 100 fs, 1 kHz) provided the 800 nm beam, which was further split to generate: (1) a 532 nm pump pulse in the optical parametric amplifier (Topas Prime with a NirUVVis frequency mixer) and (2) a white light continuum probe pulse in a sapphire crystal (430–780 nm). The remaining 800 nm probe pulse photons were filtered just after white light continuum generation. The instrument response function (IRF) was estimated to be around 110 fs (FWHM). The pump diameter (FWHM) at the sample was approximately 250 µm, for a pulse energy of 0.8 µJ. Absorbance was close to 0.7 at the excitation wavelength over a 2 mm optical path (55 µM or 1.9 mg/mL). The sample solution was stirred to keep the OCP solution fresh in the probed volume. The pump beam was depolarized to avoid anisotropy effects. To ensure that datasets are comparable to each other, they were all measured under identical conditions (at 22°C) during a single experimental session. The transient absorption data were corrected for the chirp of white light continuum by aligning kinetics according to a delay introduced by given amount of the material between the OCP sample and the sapphire crystal (used for WLC generation of the probe). For all datasets, the difference absorbance (ΔA) value obtained at the bleaching extremum (in both spectral and temporal dimension) was normalized to -1. Transient spectra were projected onto a 5 nm-spaced grid to get kinetic traces. The comparison of pre-exponential factors at 490 nm (bleaching band) allowed us to estimate the quantum yield of the formation of the various intermediates. We used for interpretation the most recent proposed model (Nizinski et al., submitted; doi.org/10.1101/2021.12.26.474187), whereby S_1, ICT and S^* are formed from S_2 in parallel paths and decay mainly to S_0 without any interconversion and with only small contribution of excited-state absorption at 490 nm. For P_1 formation quantum yield, the positive absorbance contribution was taken into account (Nizinski et al., submitted; doi.org/10.1101/2021.12.26.474187). Time constants determination and calculation of Decay Associated Difference Spectra (DADS or DAS) were achieved by global analysis using our custom-Python package (Nizinski et al., submitted; doi.org/10.1101/2021.12.26.474187) and the Glotaran software (https://glotaran.org). For the global analyses, a sum of four exponentials (S_2, ICT, S_1, S^*) convolved by a Gaussian IRF

(fixed to 110 fs) and an offset (representing long-lived photo-products with lifetime > 50 ns, namely P_1) was used.

Nanosecond transient absorption spectroscopy (50 ns – 1 s timescale)

Measurements were performed with our custom apparatus described previously [44]. 532 nm nanosecond excitation pump pulses of 5 mJ energy were used (one pulse every 20 s for 100 ms kinetics, one pulse every 40 s for kinetics over 100 ms). The probe light from the Xenon lamp was filtered using a 550 nm interference filter (10 nm FWHM) placed before the sample. Scattered pump light was removed by a notch filter set after the sample. For each experiment, a solution of OCP with absorbance close to 0.7 at excitation wavelength (1 cm path-length, 11 μM or 0.39 mg/mL) was placed in a 10×10mm cuvette and thermalized at 22°C. No stirring of the sample was applied, enabling to stretch the time window covered by the experiments. Each set of measurements included 100 replicates of each of the five time-windows together covering the 50 ns – 1 s time range. Recorded data were merged and projected onto a logarithmic grid. Stability of the protein was checked by its steady-state absorbance after each experiment. The formation quantum yield of OCP^R was determined using ruthenium as actinometer [45]. The difference molar absorption coefficient at 550 nm for OCP^R was estimated using the molar absorption coefficient (ε) of OCP^O at 490 nm = 63000 cm^{-1}.M^{-1}) [41] and that determined for OCP^R after 100 % photo-conversion at 8°C ($\varepsilon_{550\ nm} \approx$ 48000, 41 000, 47 000 and 40 000 cm^{-1}.M^{-1} for Syn-OCP^R_{CAN}, Syn-OCP^R_{ECN}, Plankto-OCP^R_{CAN} and Plankto-OCP^R_{ECN}, respectively). For each sample, data were fit globally over the five time- windows using a three-exponential model accounting for three different intermediates states and an offset, attributed to OCP^R, and therefore used to estimate the yield. Fitted results are shown in Table 1.

Crystallization

The N-tagged ECN-functionalized OCP from *Planktothrix aghardii* (Plankto-OCP_{ECN}), purified on Ni-NTA and phenyl-sepharose columns, was further subjected to size exclusion chromatography under dim red light (HiLoad 16/600 Superdex 75 pg, GE Healthcare). The protein eluted as a unique peak in 50 mM Tris-HCl buffer pH 7.4, 150 mM NaCl. Crystallization conditions were screened manually, using as starting conditions those that afforded crystallization of Syn-OCP [17] and *Arthrospira maxima* OCP [8]. The gel-filtrated Plankto-OCP_{ECN} sample was concentrated to 5.2, 6.6 and 7.0 mg/mL (the protein concentration was determined based on the absorption at 495 nm, using an extinction coefficient of 63 000 M^{-1} cm^{-1} [41]) and crystallization trials were performed in 24-well Limbro plates using the vapor diffusion method in the hanging-drop geometry. Crystallization drops were set at 4°C by mixing 1 μL from the well solution with 1 μL of protein solution. The well solution, of 1 mL volume, was

composed of 0.1 M or 0.2 M Bis-Tris pH 5.5 and increasing PEG 3550 concentrations (from 18% to 25%) were tested. Crystals appeared within 3 to 5 months in 0.2 M Bis-Tris pH 5.5, 20%-25% PEG 3550. Following this success, crystallization trials were optimized enabling growth of crystals in a few hours to few days at room-temperature (~20 °C). Crystallization of Plankto-OCP$_{CAN}$ was achieved using a protein concentration of 1.5 – 2 mg/ml in 50 mM Tris-HCl pH 7.4, 150 mM NaCl, a well solution composed of 0.1 M sodium acetate, pH 5 and 20-25% PEG4000, and by mixing these at 1:1 ratio in the crystallization drops.

X-ray data collection and processing and structure determination

X-ray data were collected at 100 K from crystals cryoprotected by a short soak in the mother liquor complemented with 18-20 % glycerol and directly frozen in the nitrogen gas stream at the European Synchrotron Radiation Facility (ESRF, Grenoble, France), at the Swiss Light Source (SLS, Villigen, Switzerland) or on the MicroMax-007 HF diffractometer (Rigaku) installed at the Max Planck Institute in Heidelberg (MPI-HD). Specifically, we used : (i) ESRF-ID23EH1, for collection of the Plankto-OCP$_{ECN}$ structure in the $P2_1$ space group (1.7 Å resolution; λ=0.979 Å; beamsize: 30 (h) x 30 (v) μm^2); (ii) ESRF-ID29, for collection of the Plankto-OCP$_{ECN}$ in the $C2$ space group (1.7 Å resolution; λ=0.976 Å; beamsize: 30 (h) x 30 (v) μm^2); (iii) SLS-X10SA (PXII), for collection of the Plankto-OCP$_{CAN}$ structures in the $P2_1$ space group (1.4 resolution; λ=0.99 Å; beamsize: 50 (h) x 10 (v) μm^2); and (iii) the MPI-HD diffractometer, for collection of the Plankto-OCP$_{CAN}$ structures in the $P2_1$ and C2 space group (1.85 Å resolution, respectively; λ=0.99 Å; beamsize: 50 (h) x 10 (v) μm^2). Data were collected with an oscillation range of 0.1 (ID29 and ID23-EH1), 0.2 (SLS-X10SA (PXII) or 0.25 degree (MPI-HD). All data were indexed using XDS [46], and scaled and merged using XSCALE [47].

Molecular replacement and structure refinement.

Phaser [48] was used to phase by molecular replacement (MR) the data collected on crystalline Plankto-OCP$_{ECN}$ in the $C2$ space group, using as a starting model chain A from the Syn-OCP$_{ECN}$ structure (PDB id: 3mg1, [17]). We used the CCP4 [49] buccaneer pipeline, based on Buccaneer [50], Parrot [51] and Refmac5 [52] for the initial *in silico* rebuilding of the $C2$ Plankto-OCP$_{ECN}$ structure (76.2% and 92.8% identity and similarity with respect to Syn-OCP), resulting in a model characterized by Rfree and Rwork values of 29.63 and 26.17, respectively, and wherein 306 residues had been placed in sequence in two fragments corresponding to the NTD and CTD. Examination of this model revealed imperfections in loop building, which were corrected manually using the molecular graphics program Coot [53]. The $C2$ Plankto-OCP$_{ECN}$ structure was thereafter refined by iterative cycles of reciprocal-space refinement using Refmac5 and manual model-building in real-space using Coot. Therefrom, phasing of the $C2$ Plankto-OCP$_{CAN}$ data was achieved by rigid-body refinement with Refmac5, while that of the

$P2_1$ Plankto-OCP$_{ECN}$ and Plankto-OCP$_{CAN}$ structures was achieved by molecular replacement with Phaser, using as a starting model the refined $C2$ Plankto-OCP$_{ECN}$ structure devoid of the carotenoid, waters and protein alternate conformations. Refinement again consisted of iterative cycles of reciprocal-space refinement using Refmac5 and manual model-building in real-space using Coot. Using $C2$ Plankto-OCP$_{CAN}$ as the reference structure, Cα-Cα distance difference matrices were prepared using a custom-written script, and the hinge motions of domains within monomers and of monomers within dimers were evaluated using hinge_find.py script available at https://github.com/gawells/hingefind, inspired from the hinge_find.tcl script [54] available at http://biomachina.org/disseminate/hingefind/hingefind.html. The presence of tunnels in OCP, and notably the extent and volume of the carotenoid binding tunnel, was examined using Caver3 [55] and the dedicated PyMOL plugin available at https://pymolwiki.org/index.php/Caver3). Porcupine plots, showing for each structure the direction and distance travelled by Cα atoms with respect to the $C2$ Plankto-OCP$_{CAN}$ structure, were prepared using the modevectors.py PyMOL script available at https://pymolwiki.org/index.php/Modevectors. Figures were prepared with PyMOL unless stated otherwise. Data processing and refinement statistics are shown in Table 2. *Planktothrix* OCP structures have been deposited in the wwPDB under accession codes 7qd0, 7qcZ, 7qd1 and 7qd2.

13

Results

Comparison of native (non-tagged) OCPs from *Planktothrix aghardii* and *Synechocystis* PCC6803

The *Synechocystis* and *Planktothrix* species share the feature that only one *ocp* gene, classified in the OCP1 clade [16], and one *frp* gene are found in their genomes. The two OCP genes display 76.2% and 92.8% identity and similarity, respectively, with nearly all residues lining the carotenoid tunnel being conserved. We investigated whether or not the functionalizing carotenoid and his-tagging have an effect on the photoactivation and recovery kinetics of these two OCP, by expressing recombinantly the native (non-tagged), N-tagged and C-tagged *Planktothrix* and *Synechocystis ocp* genes in CAN or ECN producing *E. coli* cells (for details on constructs and on their expression and purification, see Materials and Methods section).

We first compared the spectral properties at 9.5 °C of the native (non-tagged) CAN-functionalized Syn-OCP and Plankto-OCP (Figure 2), viz. Syn-OCP$_{CAN}$ and Plankto-OCP$_{CAN}$. The two proteins display identical absorption spectra in the dark-adapted (orange) inactive state (OCP^O), however slight differences are seen for the light-adapted (red) active state (OCP^R) (Figures 2A, D and Supplementary Figure 1). Both OCP$^R_{CAN}$ spectra present an absorption maximum at 530 nm with a shoulder at 560 nm. This shoulder is slightly more pronounced in Syn-OCP$^R_{CAN}$. (Figures 2A and 2D). A difference positive absorbance maximum at 560 nm is observed in both OCPs (Figures 2B and 2E). The normalization of the difference spectra time series on the 470 nm peak not only confirms that the ΔA (560 nm) to ΔA (470 nm) ratio is higher in Syn-OCP$^R_{CAN}$ than in Plankto-OCP$^R_{CAN}$ (Figures 2C and 2F), but also evidences a red shift in the spectra of both OCP^R (from 545 - 550 to 560 nm) as they accumulate (Figures 2C and 2F).

We then assayed photoactivation and thermal recovery kinetics of Syn-OCP$_{CAN}$ and Plankto-OCP$_{CAN}$ (Figure 2G and H). Experiments were performed at 9.5°C, to minimize the negative contribution of thermal recovery to the steady-state accumulation of OCP^R – *i.e.*, to maximize OCP^R concentration in the photostationary equilibrium. Accumulation of OCP^R was monitored by following the rise in absorbance at 550 nm upon intense white-light illumination. Results in Figure 2 show that Plankto-OCP$^R_{CAN}$ not only accumulates significantly faster than Syn-OCP$^R_{CAN}$ (initial slope is twice as high), but it also recovers the dark OCP^O state faster. Indeed, Plankto-OCP$^R_{CAN}$ recovers fully within the 20 min lapse of our experiment (Figure 2H), whereas only 30 % of Syn-OCP^R has reconverted to OCP^O. The slow recovery kinetics at low temperature of Syn-OCP$^R_{CAN}$ is known, and shared by other OCP1s from *Arthrospira* and *Tolypothrix* [15, 16, 42], whereas the fast recovery kinetics of Plankto-OCP$^R_{CAN}$ is

14

unprecedented for members of the OCP1 clade. It is reminiscent of those displayed by members of the OCP2 [14, 16] and OCPX [16] clades. In these clades, the faster OCP^R-to-OCP^O recovery rate coincides with the inability to interact with FRP [15, 16]. Therefore, we challenged a possible misclassification of Plankto-OCP as a member of the OCP1 clade by investigating whether or not its recovery is accelerated by the presence of FRP. For this purpose, *Synechocystis* and *Planktothrix* FRPs were expressed and purified, and assayed for their species-specific effect on the CAN-functionalized native versions of OCP. Figure 2I shows that the presence of FRP accelerates the recovery rate of Plankto-OCP$_{CAN}$ although the observed acceleration is smaller than for Syn-OCP$_{CAN}$ in presence of Syn-FRP. These results confirm the correct assignment of Plankto-OCP to the OCP1 clade. They also show that the species-specific acceleration by FRP of OCP recovery is independent of the rate of the reaction in the absence of FRP.
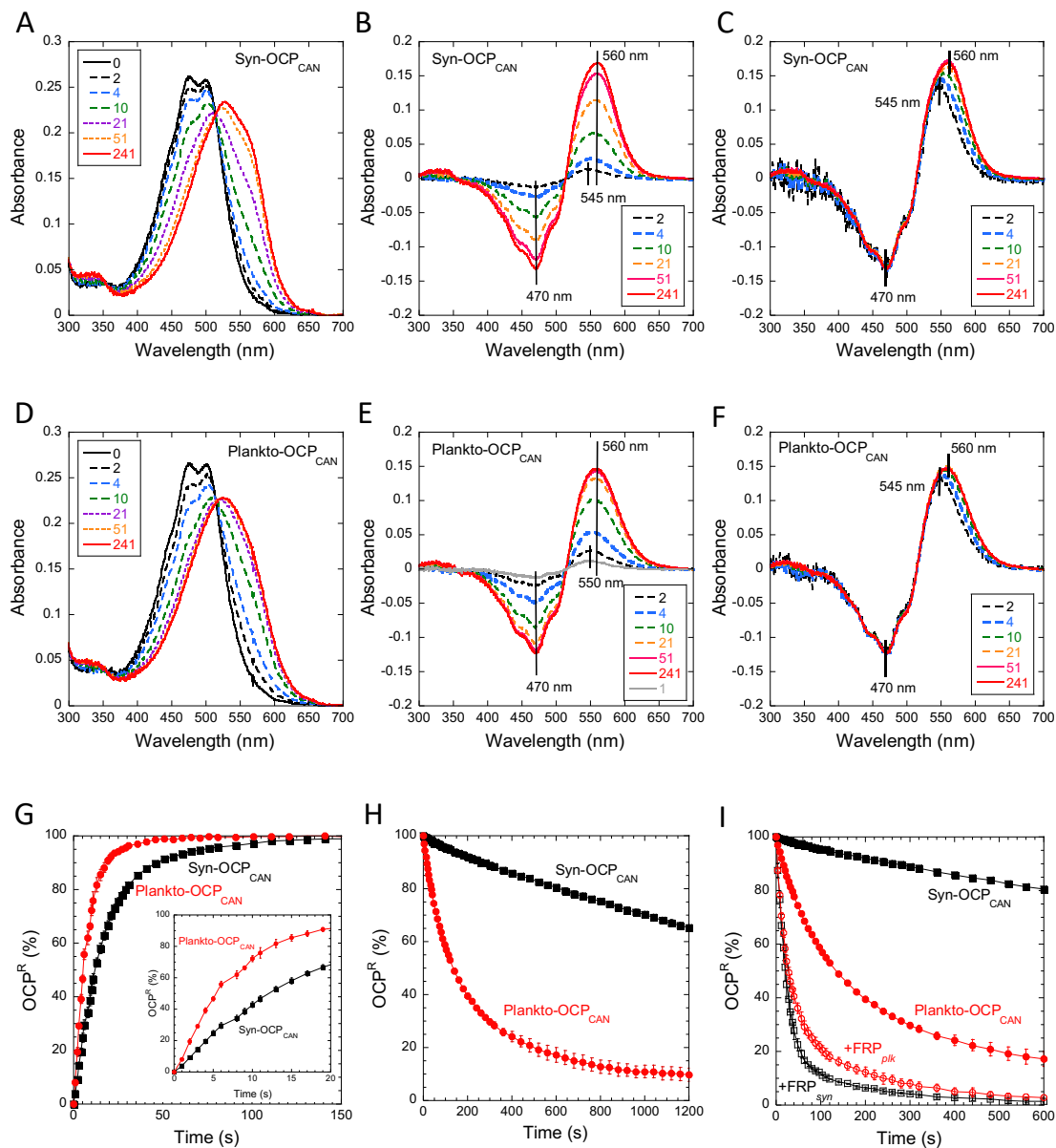
Figure 2: Photoactivation and recovery of native (non-tagged) CAN-functionalized *Synechocystis* and *Planktothrix* OCPs. (A and D) Absorbance spectra of Syn-OCP$_{CAN}$ (A) and Plankto-OCP$_{CAN}$ (D) at different times of illumination. (B and E) Differential absorbance spectra derived from A and D respectively. (C and F) Differential absorbance spectra normalized at 470 nm derived from A and D. (G-I) Kinetics of photoactivation (G) and recovery (H-I) of CAN-functionalized Syn-OCP (black) and Plankto-OCP (red). Inset in G: First 30 s of illumination. In (I), the effect of the presence of FRP is shown. The ratio FRP to OCP was 1:1. The accumulation of OCP^R and its thermal deactivation were followed by increase and decrease of absorbance at 550 nm. The OCPs were illuminated with white light (5 000 µmol photons m^{-2}. s^{-1}) at 9.5°C. Error bars: standard deviation. Each curve represents the mean of three independent measurements, respectively.

Influence of the His-tag on OCP photoactivation and recovery kinetics

We have recently shown that the location of the His-tag influences the photoactivation speed (initial slope) in *Synechocystis* OCP (Nizinski et al., submitted; doi.org/10.1101/2021.12.26.474187). In particular, by using intermediary light intensity (~100 µmol photons.m^{-2}. s^{-1}) we observed a more efficient accumulation of OCP^R in Ntag-Syn-OCP$_{ECN}$ than in Ctag-Syn-OCP$_{ECN}$ despite a comparable P1 formation quantum yield. Hence, we here asked whether or not presence of a His-tag, and its location at the N- or C-terminus, would influence the photoactivation and thermal recovery of Plankto-OCP and Syn-OCP. We compared results obtained from the N-tagged (Ntag-Syn-OCP$_{CAN}$ and Ntag-Plankto-OCP$_{CAN}$) and C-tagged (Ctag-Syn-OCP$_{CAN}$ and Ctag-Plankto-OCP$_{CAN}$) variants of these OCPs to those of the native counterparts. It was consistently observed that the N-tagged OCPs photoactivate faster than their C-tagged counterparts, with the native variants showing an intermediary behavior (Figure 3A and 3B). Nevertheless, when triggered with 5 000 µmol photons m^{-2}. s^{-1} white light, the effect of tagging on photoactivation was not dramatic. Focusing next on the thermal OCP^R to OCP^O recovery, we found that it is delayed by presence of a His-tag in all tested OCPs (Figures 3C and 3D), although the effect is clearly more visible for Plankto-OCP$_{CAN}$, which recovers faster than Syn-OCP$_{CAN}$. Introduction of a His-tag at the N-terminus hardly effects the recovery of Plankto-OCP, whereas that at the C-terminus slows down the recovery by a factor of six (Figure 3D). In contrast, in Syn-OCP, His-tagging only has a slight effect on recovery.

Influence of the functionalizing carotenoid on OCP photoactivation and recovery kinetics

We then investigated the extent to which photoactivation and thermal recovery are affected by the type of functionalizing carotenoid. As it was found above that N-tagged and native OCP are the most similar in terms of photoactivation and recovery rates, we used N-tagged Syn-OCP and Plankto-OCP in the following assays. Irrespective of the species, OCP^R accumulation is slower in ECN-functionalized than CAN-functionalized OCP (Figures 4A and 4B), while recovery is faster (Figure 4C and 4D). For example, the initial slopes of OCP^R accumulation

by Ntag-Syn-OCP$_{CAN}$ and Ntag-Plankto-OCP$_{CAN}$ are twice as high as those measured on their ECN-functionalized counterparts (Figures 4A and 4B). The most straightforward explanation for these observations is that CAN stabilizes OCP^R and/or facilitate the carotenoid translocation during photoactivation. The red Syn-OCP$_{ECN}$ and Plankto-OCP$_{ECN}$ are spectrally similar, both presenting a maximum absorption at 510 nm (Figures 4E and H). In difference absorption spectra, the positive maximum is yet at 550.5 nm, *i.e.,* slightly blue shifted compared to the OCP$_{CAN}$ counterparts (Figure 2 and Figures 4F, I). It is notable that an increase in the ΔA (550 nm) to ΔA (470 nm) ratio is observed in the first 10 seconds of illumination of Plankto-OCP$_{ECN}$ (Figure 4J); such an effect is not seen with Syn-OCP$_{ECN}$ (Figure 4G).
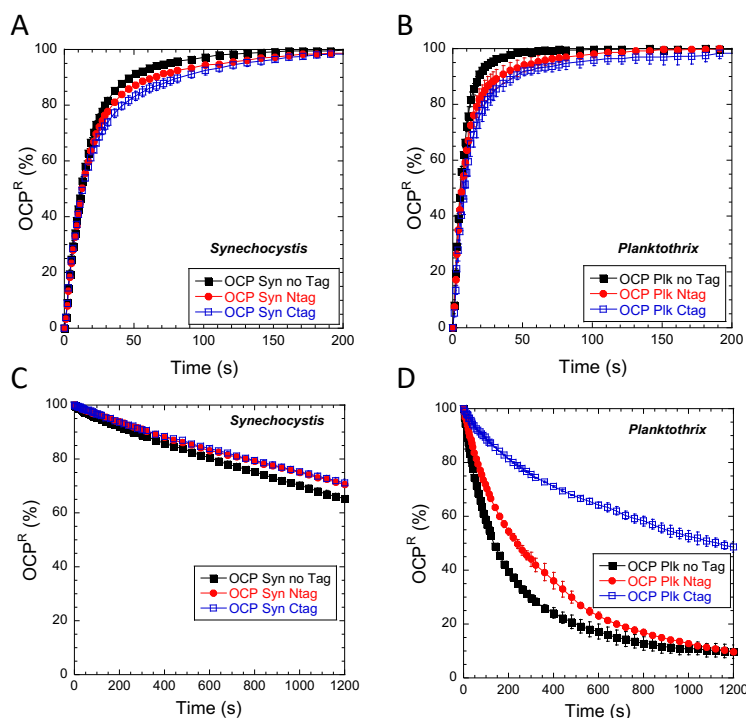

Figure 3: Presence of a His-tag has an impact on photoactivation and recovery. Effect of presence and position of His-tag on photoactivation (A-B) and recovery (C-D) of CAN-functionalized *Synechocystis* and *Planktothrix* OCPs. The accumulation of OCP^R and its thermal deactivation were followed by increase and decrease of absorbance at 550 nm. The OCPs were illuminated with white light (5 000 µmol photons m^{-2}. s^{-1}) at 9.5°C. Error bars: standard deviation. Each curve represents the mean of three independent measurements.

By carrying out fs-ns timescale transient absorption spectroscopy on the four OCPs, we inquired whether or not the increased photoactivation speed of CAN-functionalized Plankto- and Syn-OCP stem from changes in the carotenoid excited state dynamics. Thereby we could estimate the primary quantum yields for the formation of the five intermediates occurring during the initial 100 fs-100 ps of the photoactivation cascade, *i.e.,* the S$_2$, S$_1$ and ICT excited-states, the S* state, and the first photoproduct P$_1$ (see Material and Methods section and Nizinski et al., submitted; doi.org/10.1101/2021.12.26.474187). Their formation and decay in CAN- and ECN-functionalized Plankto-OCP (Figure 5) and Syn-OCP (Supplementary Figure 2) were monitored by recording and globally-fitting femtosecond transient spectra collected at different

time delays following a 110-fs pulse excitation at 532 nm (see the Materials and Methods section for further details).
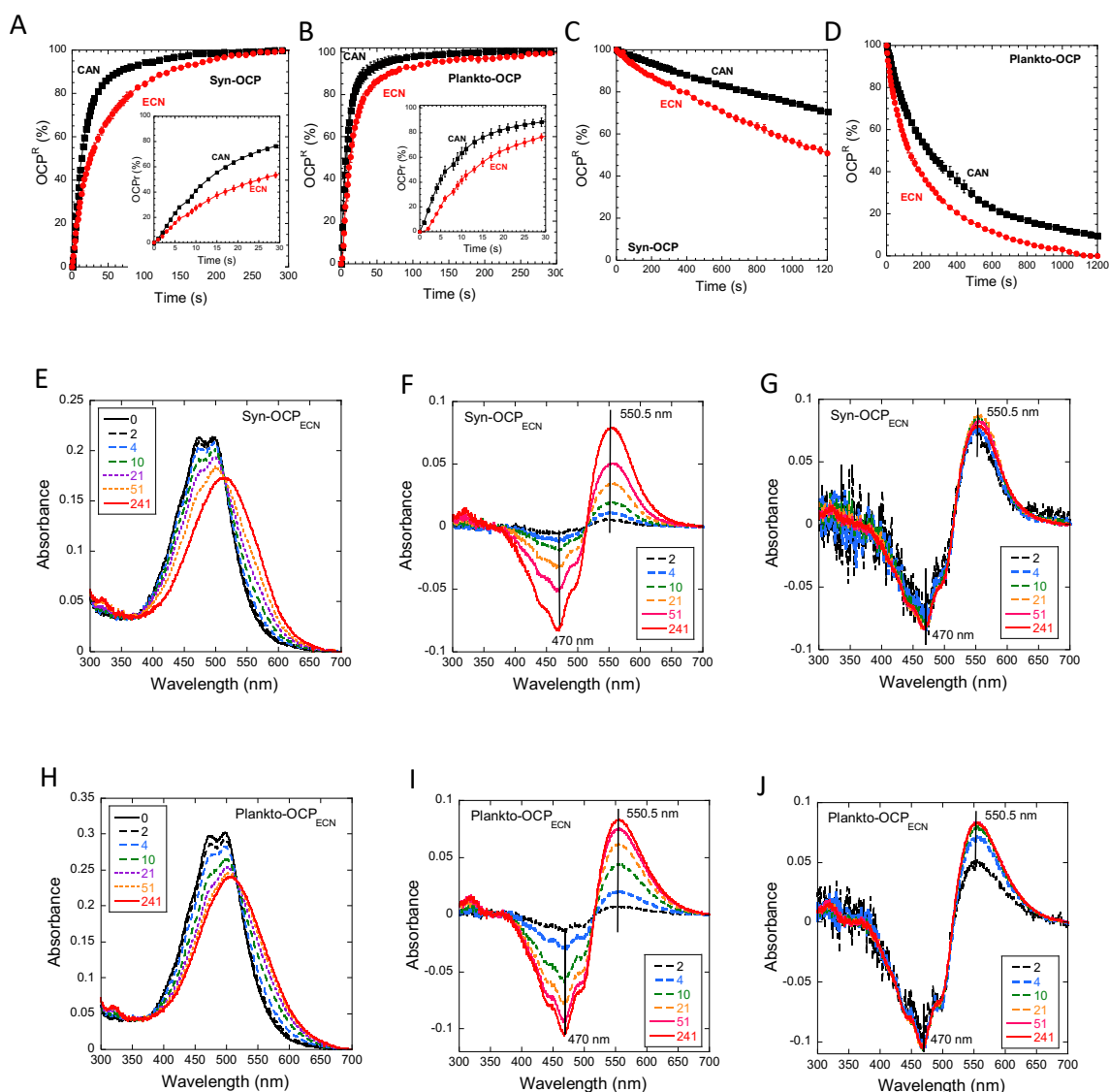

Figure 4: Effect of the nature of the functionalizing ketocarotenoid on photoactivation and recovery of N-terminus His-tagged *Synechocystis* and *Planktothrix* OCPs. (A-B) Kinetics of photoactivation of Syn-OCPs (A) and Plankto-OCPs (B) functionalized with ECN (red) or CAN (black). Inset in A and B: First 30 s of illumination. The OCPs were illuminated with white light (5 000 µmol photons m^{-2}. s^{-1}) at 9.5°C. (C and D) Thermal recovery of OCP^R in darkness of Syn-OCPs (C) and Plankto-OCPs (D) functionalized with ECN (red) or CAN (black). The accumulation of OCP^R and its thermal recovery were followed by increase and decrease of absorbance at 550 n, respectively. Error bars: standard deviation. Each curve represents the mean of three independent measurements, respectively (E and H) Absorbance spectra of ECN-Syn (E) and ECN-Plankto OCPs (H) at different times of illumination. (F and I) Raw difference absorbance spectra derived from E and H respectively. (G and J) Difference absorbance spectra derived from E and H, respectively, after normalization on the 470 nm band.

In agreement with previous reports, we found that 0.15 ps after excitation, the S$_2$ excited state has already started to decay. Transient absorption spectra are characterized by a ground state bleaching (GSB) negative band with an extremum at ≈ 500 nm, indicative of OCP^O

depopulation, and by positive absorption (ESA) bands for the S_1, ICT and S^* states peaking at ≈ 660 nm, ≈ 750 nm and ≈ 575 nm (shoulder), respectively. All excited- and vibrationally-hot ground-states have decayed by the 30 ps time-delay, and only a broad positive band centered at ≈ 560 nm, previously assigned to the photoproduct P_1 [19] (Nizinski et al., submitted; doi.org/10.1101/2021.12.26.474187), can be seen at the 95 ps time delay. P_1 shows no spectral evolution in our experimental time window, *i.e.,* up to 1 ns time delay.
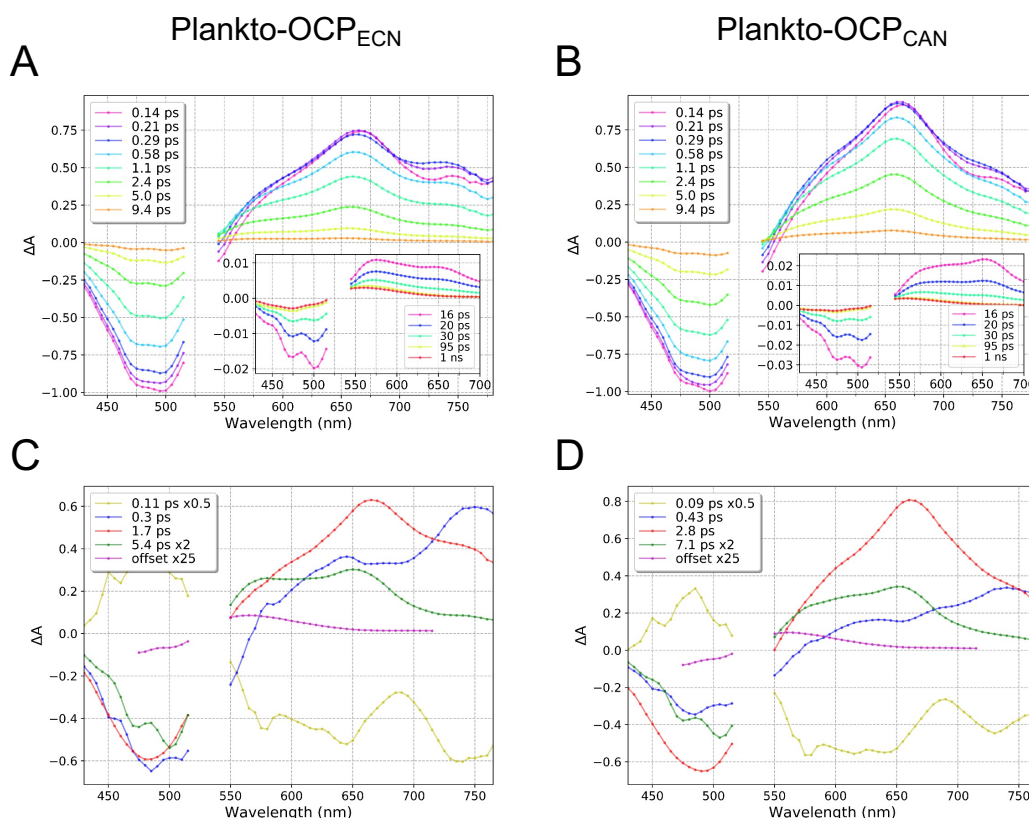

Figure 5: Femtosecond transient absorption data collected on the Ntag-Plankto-OCP. (A, B) Transient absorption spectra measured after excitation at 532 nm are shown for time delays ranging between 0.14 and 1 ns for (A) Ntag-Plankto-OCP$_{ECN}$ and (B) Ntag-Plankto-OCP$_{CAN}$. All datasets were normalized to -1 at bleaching minimum, in both spectral and temporal dimensions. (C, D) Decay Associated Spectra (DAS) obtained from the global fit of the transient absorption data spectra shown in (A) and (B), respectively. Data were fitted using four exponential components convolved by a Gaussian pulse (IRF, 110 fs FWHM) and an offset (long-lived photo-product > 10 ns).

Four exponential components (S_2, ICT, S_1 and S^*) and one offset (P_1) were accounted for in the global decay analysis, enabling to extract the decay associated spectra (DAS) and lifetimes of the various intermediate states in ECN- and CAN- functionalized Plankto-OCP (Figure 5C and 5D) and Syn-OCP (Supplementary Figure 2C and D). Note that the DAS associated with the shortest time-constants is estimated from a convolution of the S_2 decay and rise of the excited-state signals, as our resolution is about 110 fs. The difference spectrum obtained ≈ 30 ps post-excitation (offset value in the sum of exponentials) is attributed to the P_1 intermediate

19

state. Using the GSB kinetics, and assuming that the S_1, ICT and S* states form from S_2 and parallelly decay to the ground state, we could further estimate the quantum yields of each, as well as of P_1. In agreement with previous reports, the picosecond excited state dynamics and yields are similar for the four tested OCPs, with similar DAS observed for the ICT (blue), S_1 (red), S* (green) and P_1 (magenta) states, respectively (Figure 5C and 5D). However, a detailed analysis of DAS for CAN and ECN-OCPs (either Plankto or Syn) shows that the value of absorbance amplitude for S_1 and ICT above 700 nm is higher for ECN, assigned to a more pronounced ICT character in the ICT and S_1 states. The characterized lifetimes are also in agreement with previous reports [59], viz. ~0.15 (± 0.1), ~0.5 (± 0.1), ~2 (± 0.5) and ~7 (± 2.5) ps for the S_2, ICT, S_1 and S* states, respectively (Figure 5 and Table 1). Thus, the lifetimes of excited-states do not vary as a function of the species or the functionalizing carotenoid. As expected from the DAS and the literature [40], the formation QY for the ICT state is lower in OCP_{CAN}. The observed P_1 yield is yet similar in the four tested OCP (≈ 0.5 ± 0. 1 %), in agreement with our recent results (Nizinski et al., submitted; doi.org/10.1101/2021.12.26.474187), as well of others [19, 23].

Having excluded the hypothesis that the type of carotenoid or OCP scaffold significantly influences the yield of P_1, we shifted our focus to the ns-s dynamics by performing nanosecond transient absorption experiments, whereby a nanosecond laser pulse is used to trigger excitation and the photoactivation outcome is probed in the 50 ns – 1 s time window by monitoring changes in the absorbance at 550 nm (Figure 6). Indeed, on these timescales, the maximum difference-absorbance varies between 563 nm, characteristic of the P_1 state, and 550 nm, signing for OCP^R. Intermediate states were assigned on the basis of earlier reports, with the P_1, P_2-P_2' and $P_3(P_N)$/P_M/P_X states displaying lifetimes of ~ 50 ns, ~ 0.5-10 μs, and ~ 1-100 ms, respectively. Recall that these states were proposed to be associated with (i) rupture of H-bonds between the carotenoid and the protein scaffold (P_1); (ii) translocation of the carotenoid from the NTD/CTD interface into the NTD (P_2-P_2', P_3); and (iii) NTE and CTT detachment (P_M) followed by dissociation of the two domains (P_X), respectively. A last conformational change thence occurs, yielding from P_X the metastable OCP^R (Figure 1). This last step could correspond to the repositioning of the CTT on the CTD-half of the carotenoid tunnel [34]. Note that partial recovery of the OCP^O state occurs at all steps (see Figure 1), explaining the decrease in absorbance at 550 nm over the probed time window.
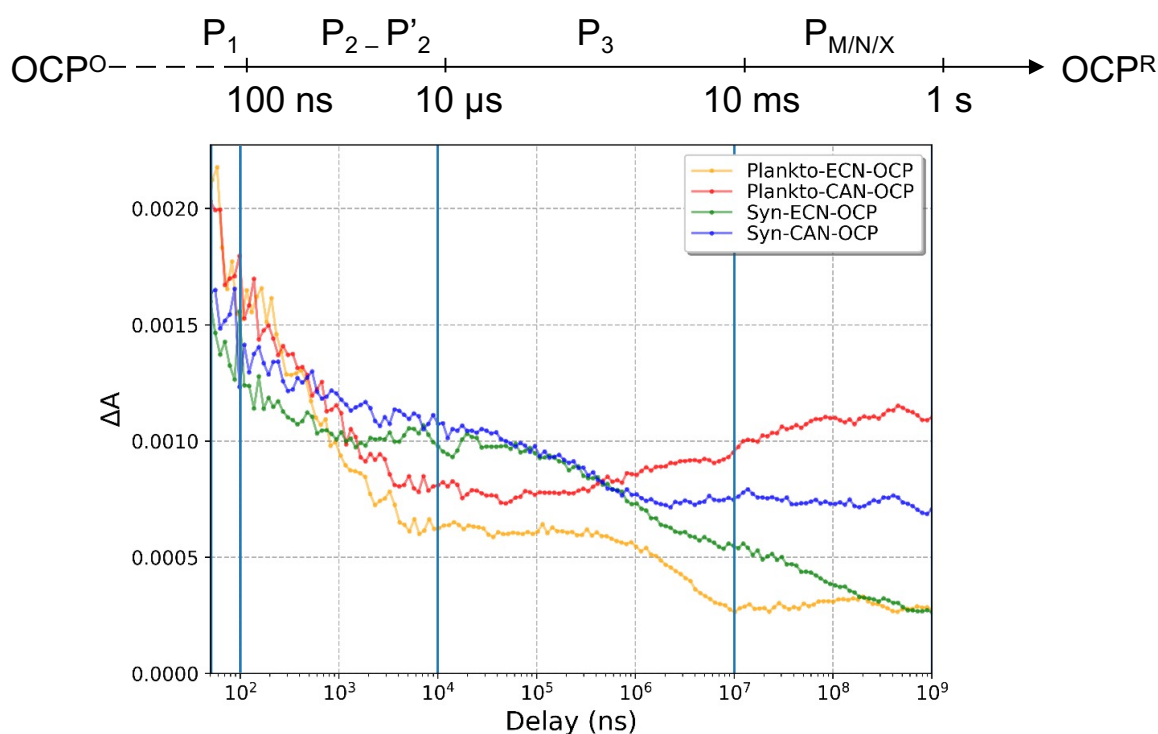
Figure 6: Nanosecond-second dynamics in CAN- and ECN-functionalized Plankto-OCP and Syn-OCP. Time evolution (50 ns to 1 s) of the difference absorption signals at 550 nm recorded on Plankto-OCP$_{ECN}$ (yellow), Plankto-OCP$_{CAN}$ (red), Syn-OCP$_{ECN}$ (green) and Syn-OCP$_{CAN}$ (blue) after excitation by a 532 nm ns-pulse. The intermediate states proposed [12, 19, 23] to underlie the observed absorption changes are indicated at the top of the figure. Measurements were carried out at 22°.

Clear differences are seen between the four tested OCPs in these experiments. First, irrespective of the carotenoid, the starting difference absorbance signal (at 50 ns) is higher for Plankto-OCP (~0.002) than for Syn-OCP (~0.0015), suggesting a higher P_1 yield (Figure 6). This result contradicts the above assumption that the P_1 yield is the same for all investigated OCPs, but can be rationalized by recalling that (i) in the fs-ns experiments, the GSB band at 490 nm is used to estimate the P_1 yield, instead of the characteristic positive absorption band at 563 nm, in the ns-s experiments; and most importantly (ii) a large fraction of P_1 reverts to the dark-adapted OCP^O state. Thus, the higher P_1 yield observed for Plankto-OCP at the start of ns-s transient absorption experiments (50 ns) could be related to a reduced recovery from P_1 of the Plankto-OCP^O state. Irrespective of the functionalizing carotenoid, the difference absorptions of Plankto-OCP and Syn-OCP drop by about 60 % and 40 % on the ns - μs time scale, respectively. The larger drop in Plankto-OCP signal could underlie sub-optimal translocation of the carotenoid into the Plankto-NTD, compared to the Syn-NTD. On the μs-s time scale, the most important differences between Plankto-OCP and Syn-OCP are visible in the μs to ms timescale, whereas differences between CAN- and ECN-functionalized OCP concentrate in the ms-s time window. Thus, both carotenoid translocation and NTE/CTT

detachments seem to be affected by the change in protein scaffold, however, it is domain dissociation that is most affected by a change in the functionalizing carotenoid. This step appears to be faster and more efficient in CAN-functionalized OCP, with a slight increase in ΔA (550 nm) being visible after 1 ms, whereas recovery to the initial state is higher for ECN-functionalized OCP, as evidenced by the decrease of ΔA (550nm). Of note, this decline is present only in ECN-functionalized OCPs, in accordance with the observation that CAN-functionalized OCP can be photoactivated more efficiently. In the case of Plankto-OCP$_{CAN}$, we observe faster domain separation and no recovery to OCP^O on the µs-s timescale (100% efficiency from P$_3$ to final OCP^R). The larger difference absorption signals observed for Plankto-OCP (most notably Plankto-OCP$_{CAN}$) on the 10 ms – 1 s time window mirror the differences in photoactivation efficiency observed in stationary irradiation experiments.

Multiscale exponential fitting was carried out to extract the lifetimes of the intermediate states (Table 1). The lifetime of the P$_1$ state was found to be almost independent of the OCP variant. For the P$_2$-P$_{2'}$ states (*i.e.,* on the 50 ns to 10 µs time scale), data were fit by one or two exponentials, depending on the case, yielding lifetimes in the order of 0.5-2 µs. Likewise, for the P$_3$/P$_N$/P$_X$ states (*i.e.,* on the 0.1-10 ms time scale), either one or two exponentials were required to fit the data, yielding lifetimes in the order of 0.1-1 ms. Note that these lifetimes are in good agreement with those reported earlier based on experiments carried out on the C-tagged Syn-OCP$_{ECN}$ [19, 23]. The experimental setup did not allow to evaluate a lifetime for OCP^R, but previous reports have pointed to the second timescale [23]. Nevertheless, our data establish that the OCP^R yield is higher for CAN-functionalized OCP, and that Plankto-OCP photoactivates more efficiently. Thus, the differences observed in the photoactivation efficiency of CAN- and ECN-functionalized Plankto- and Syn-OCP stem from evolutions observed during the (comparatively-slow) carotenoid translocation, NTE/CTT detachment and domain dissociation steps – but not from changes in the excited-state dynamics of the OCP-embedded carotenoid.

Interaction between OCP and the phycobilisome

We then inquired the energy-quenching performance of the various ECN- and CAN-functionalized OCPs, focusing on OCP and PBS from *Synechocystis* and *Planktothrix*. The PBS from *Synechocystis* has been well characterized in several laboratories including ours [42, 56]. However, no information was available regarding the *Planktothrix* PBS, requiring us to first characterize it biochemically (Supplementary Figure 3). We found that similar to *Synechocystis* PBS, *Planktothrix* PBS consists of a core (formed by three cylinders containing four allophycocyanin (APC) trimers) from which radiate six rods constituted of three phycocyanin (PC) hexamers.

With this characterization in hand, we pursued the investigation of native Syn-OCP and Plankto-OCP energy-quenching activities, focusing first on the effect of the functionalizing-carotenoid (Figure 7) in species-specific OCP/PBS complexes. The decrease of PBS fluorescence was followed using a PAM fluorimeter during incubation of PBS under strong blue-green light and in presence of pre-photoactivated OCPs. Under these conditions, a faster and larger decrease of fluorescence is suggestive of a stronger OCP-PBS interaction. We found that native Syn-OCP$_{CAN}$ and Syn-OCP$_{ECN}$ induce similar Syn-PBS fluorescence quenching (~75 % of PBS fluorescence is quenched after 300 s), despite a slightly lower initial rate for native-Syn-OCP$_{CAN}$ suggesting a weaker binding to the PBS (Figure 7A). This hypothesis was confirmed by the eight times faster PBS fluorescence recovery observed for native-Syn-OCP$_{CAN}$, as compared to native-Syn-OCP$_{ECN}$ (Figure 7B). The nature of the functionalizing-carotenoid also had an effect on native-Plankto-OCP quenching efficiency and on the Plankto-PBS fluorescence recovery rate. PBS fluorescence quenching was twice more efficient with native-Plankto-OCP$_{ECN}$ than with native-Plankto-OCP$_{CAN}$ (75 and 40 % of fluorescence quenching after 300 s incubation, respectively). In line with the hypothesis that this variance originates from a reduced affinity for the PBS of CAN-functionalized OCPs, fluorescence recovery was nearly three times faster for native-Plankto-OCP$_{CAN}$ than native-Plankto-OCP$_{ECN}$.
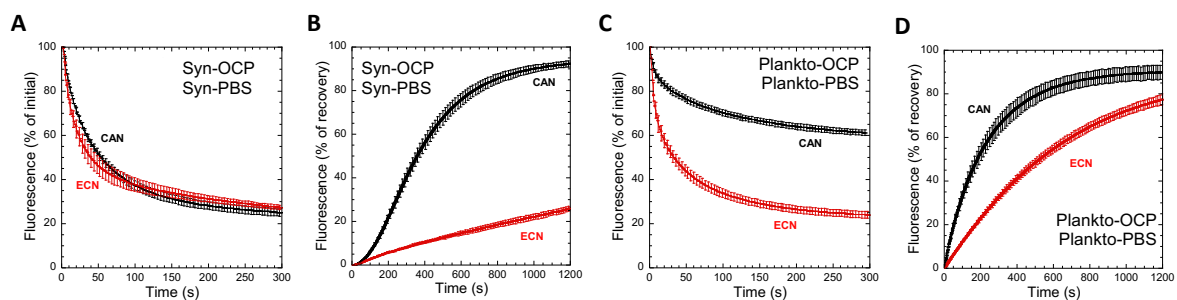

Figure 7: Effect of ketocarotenoid on OCP-PBS interaction. (A, C) *Synechocystis* (A) and *Planktothrix* (C) PBS fluorescence quenching induced at 23°C in 0.5 M phosphate buffer by CAN (black) and ECN (red) functionalized *Synechocystis* (A) and *Planktothrix* (C) native (non-tagged) OCPs. The OCP was pre-photoactivated by illumination with a strong white light (5 000 µmol photons m^{-2}. s^{-1}) at 4°C. The ratio OCP:PBS was 40:1. (B, D) Dark recovery of fluorescence in *Synechocystis* (B) and *Planktothrix* (D) phycobilisomes. 100% of fluorescence in all graphs is the initial fluorescence of phycobilisomes without quenching. Error bars: standard deviation. Each curve represents the mean of three independent measurements.

We also investigated the effect of a His-tag, present either at the N- or C-terminus, on the species-specific PBS-fluorescence quenching efficiency and recovery rate (Figure 8). We found that irrespective of the species (*i.e.* for both Syn-OCP + Syn-PBS and Plankto-OCP + Plankto-PBS), His-tagged OCPs are more efficient at inducing PBS-fluorescence quenching,

with C-tagged OCP further surpassing the N-tagged variants (Figure 8A and 8B). This effect is most clear when considering the native, N-tagged and C-tagged Plankto-OCP/PBS complexes. A possible rationalization could come from the higher stabilization of the C-tagged OCP^R state. However, this stabilization is not sufficient to explain the observed drastic difference in PBS fluorescence-recovery rates. Indeed, up to 20 % of the initial PBS fluorescence is recovered after 20 min incubation in the dark with the C-tagged Plankto-OCP, which is at variance with the full recoveries observed when native or N-tagged Plankto-OCP and Syn-OCP are used. Thus, the C-terminal His-tag not only stabilizes OCP^R, but also the OCP^R - PBS complex.
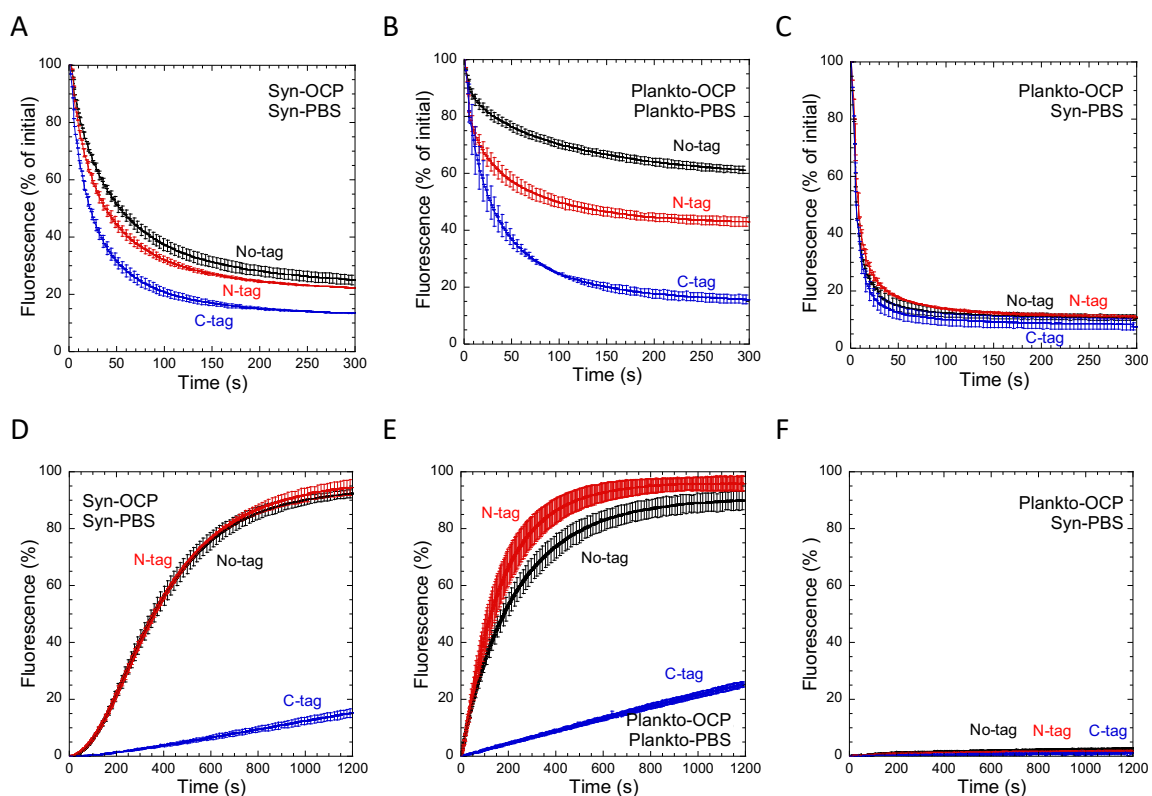

Figure 8: Effect of the presence and position of a His-tag on OCP-PBS interaction. (A-C) *Synechocystis* (A, C) and *Planktothrix* (B) PBS fluorescence quenching induced at 23°C in 0.5 M phosphate buffer by native (non-tagged; black), N-tagged (red) and C- tagged (blue) CAN-functionalized *Synechocystis* (A) and *Planktothrix* (B, C) OCPs. The OCP was pre-photoactivated by illumination of strong white light (5 000 μmol photons m^{-2}. s^{-1}) at 4°C. The ratio OCP:PBS was 40:1. (D-F) Dark recovery of fluorescence in *Synechocystis* (D, F) and *Planktothrix* (E) PBS. 100 % of fluorescence in all graphs is the initial fluorescence of phycobilisomes without quenching. Error bars: standard deviation. Each curve represents the mean of three independent measurements.

In the past, we demonstrated that *Synechocystis*, *Arthrospira* and *Anabaena* OCPs bind more strongly to the *Synechocystis* PBS than to the *Anabaena* or *Arthrospira* PBS [42], with *Synechocystis* OCP binding comparatively weakly to the PBS from other species [42]. Hence, we asked whether or not these conclusions hold as well for *Planktothrix* OCP and PBS. We

24

found that irrespective of the presence and position of the His-tag, *Planktothrix* OCP binds more strongly to *Synechocystis* PBS than to *Planktothrix* PBS, with all Plankto-OCPs inducing a faster and more efficient fluorescence quenching of Syn-PBS (Figure 8B) compared to Plankto-PBS (Figure 8C). Furthermore, the *Synechocystis* PBS fluorescence recovery was virtually null, indicating that the complex formed by Plankto-OCP and Synechocystis-PBS is highly-stable at 0.5 M phosphate (Figure 8F). Contrastingly, Syn-OCP was unable to induce *Planktothrix* PBS fluorescence even at higher phosphate concentrations (till 1.4 M phosphate), suggesting that it is able to interact only with *Synechocystis* PBS.

Structures of CAN- and ECN-functionalized *Planktothrix* OCP reveal new features.
The crystal structures of *Synechocystis* PCC 6803 (PDB id: 4xb5), *Anabaena* PCC 7120 (PDB id: 5hgr; also referred to as *Nostoc*), *Tolypothrix* PCC 7601 (PDB id: 6pq1; also referred to as *Fremyella diplosiphon*) OCP have been solved in the CAN-functionalized states, while those of *Synechocystis* PCC 6803 (PDB id: 3mg1) and *Arthrospira maxima* (PDB id: 5ui2; also referred to as *Limnospira*) were determined in the ECN and hECN functionalized states, respectively. Structural comparison of these could allow to rationalize the faster and more efficient photoactivation observed for CAN-functionalized OCP in transient absorption (Figure 6) and photostationary experiments (Figure 4). Structural information on *Planktothrix* OCP is yet absent, preventing identification of the structural features that could underlie its functional characteristics – notably, the thwarted translocation of carotenoids into the NTD, revealed by transient absorption spectroscopy, and the increased photoactivation rate and lower stability of its OCP^R state, revealed by photo-stationary experiments (Figures 4 and 6).

Hence, we set to characterize the structure of Ntag-Plankto-OCP in the CAN- and ECN-functionalized states. The structure was solved, for each of these, in two space groups, viz. *C*2 and *P*2$_1$, revealing a remarkable conservation of the secondary structure (Figure 9A). The *C*2 structures were solved at slightly higher resolution (1.4 and 1.7 Å resolution for Ntag-Plankto-OCP$_{CAN}$ and Ntag-Plankto-OCP$_{ECN}$, respectively) than the *P*2$_1$ structures (1.8 Å resolution for both OCPs) (Table 2). In the *P*2$_1$ space group, the asymmetric unit features the dimer that has been observed in previous structures [8, 17, 21, 30, 57-59] and was identified as naturally-occurring *in vitro* [60] with a dissociation constant in the order of 17 µM depending on reports [16]. The large dimerization interface (1046.7 and 1084.7 Å^2 of buried surface area (BSA) in the *P*2$_1$ structures of Plankto-OCP$_{CAN}$ and Plankto-OCP$_{ECN}$) is mainly supported by N-terminal helices αA (NTE) and αB, which contribute ~70 % of the BSA, with minor contributions from helix αH (~ 20 % of the BSA) and the αE-αF and β2-β3 loops (~ 10 % of the BSA) (Figure 9B, C and Supplementary Table S1). Interestingly, the relative contributions of αA and αB to the BSA at the dimerization interface vary depending on the functionalizing

carotenoid, amounting to 37 and 33 % in Plankto-OCP$_{CAN}$, and 27 and 40 %, in Plankto-OCP$_{ECN}$, respectively. Additionally, two H-bonds fixing αA and αB from facing monomers in the Plankto-OCP$_{CAN}$ dimer (viz. R9(NH2)–Q30(O) and R9(NH1)–L31(O)) are suppressed in the Plankto-OCP$_{ECN}$ dimer (Figure 9D and Supplementary Table S1). Thus, the NTE (αA) is less constrained (BSA decreases by 25%) at the dimerization interface in the $P2_1$ Plankto-OCP$_{ECN}$ structure than in the $P2_1$ Plankto-OCP$_{CAN}$ structure, but the dimer is more tightly packed, with 25, 41 and 52 % increase in the BSA contributed by αB (largest contributor to the dimerization interface in all structures), and the αE-αF and β2-β3 loops, respectively (Supplementary Table S1). The rest of the H-bonding network at the dimerization interface is overall conserved in the $P2_1$ structures, with 3 H-bonds between αB and the facing αH (N14(OD1)–A133(N), T15(O)–N134(ND2), T17(OG1)–N134(ND2)), one H-bond between αA and the facing αEF loop (either D6(OD2)–T90(OG1) or D6(OD2)–N88(ND2) in the Plankto-OCP$_{CAN}$ and Plankto-OCP$_{ECN}$ structures, respectively) and a salt-bridge between facing αB residues (D19(OD2)-R27(NE)) (Supplementary Figures 4 and 5).

In the $C2$ structures, the dimerization interface is crystallographic (-x, y, -z) and at the origin of the two-fold symmetry of the crystals. The BSA at the dimerization interface amounts to 1061 and 1023 Å^2 in the Plankto-OCP$_{CAN}$ and Plankto-OCP$_{ECN}$ structures, respectively (Supplementary Table S1). We note that in the $C2$ structures, the relative contributions of αA and αB to the BSA at the dimerization interface hardly vary depending on the functionalizing carotenoid, amounting to respectively 32 and 40 % in Plankto-OCP$_{CAN}$, and 30 and 42 %, in Plankto-OCP$_{ECN}$ (Supplementary Table S1). Nonetheless, alike in the $P2_1$ structures, the two H-bonds affixing αA and αB from facing monomers in the $C2$ Plankto-OCP$_{CAN}$ dimer, *i.e.,* R9(NH2)-Q30(O) and R9(NH1)-L31(O), are absent in the $C2$ Plankto-OCP$_{ECN}$ dimer. Thus, these H-bonds are present in both the $P2_1$ and $C2$ Plankto-OCP$_{CAN}$ structures, but in neither of the Plankto-OCP$_{ECN}$ structures. The rest of the H-bonding network at the dimerization interface is again overall preserved in the two $C2$ structures, with two to three H-bonds between αA and the facing αH (T15(O)-N134(ND2) and T17(OG1)-N134(ND2) in the two structures, and N14(OD1) to A133(N) in the Plankto-OCP$_{CAN}$ structure only), one H-bond between αA and the facing αE-αF loop (D6(OD2)-T90(OG1) in the two structures and a salt-bridge between facing αB residues (D19(OD2)-R27(NE)) (Figure 9D). The latter salt-bridge is preserved among all OCP structures reported thus far, suggesting that it is a defining interaction in the naturally-occurring OCP dimer. Indeed, it was shown that mutation into a leucine of R27 yields a constitutively monomeric OCP [16]. The extent of the biological dimerization interface is also overall preserved among all available OCP structures including ours, with a mean BSA of 1051 ± 90 Å^2 (viz. 6pq1, 5ui2, 5hgr, 3mg1, 4xb5, and 7qd0, 7qcZ, 7qd1 and 7qd2). In this context,

two structures stand out, viz. the *Tolypothrix* OCP$_{CAN}$ and *Arthrospira* OCP$_{hECN}$ structures, with BSA of 857.9 and 1186.1 Å^2, respectively (Supplementary Tables S1 and S2).
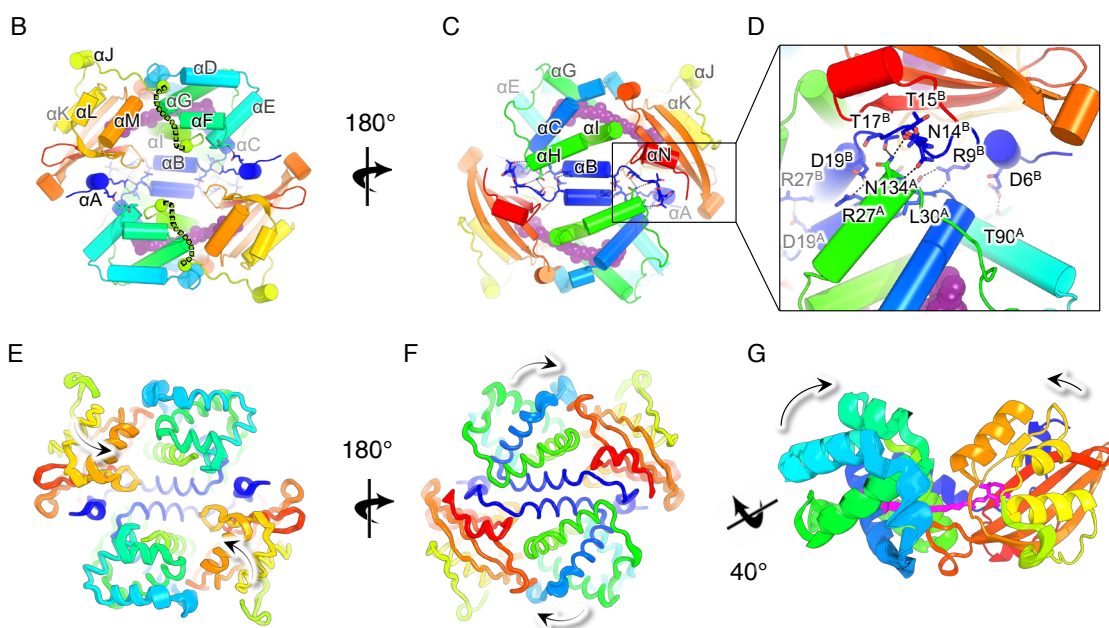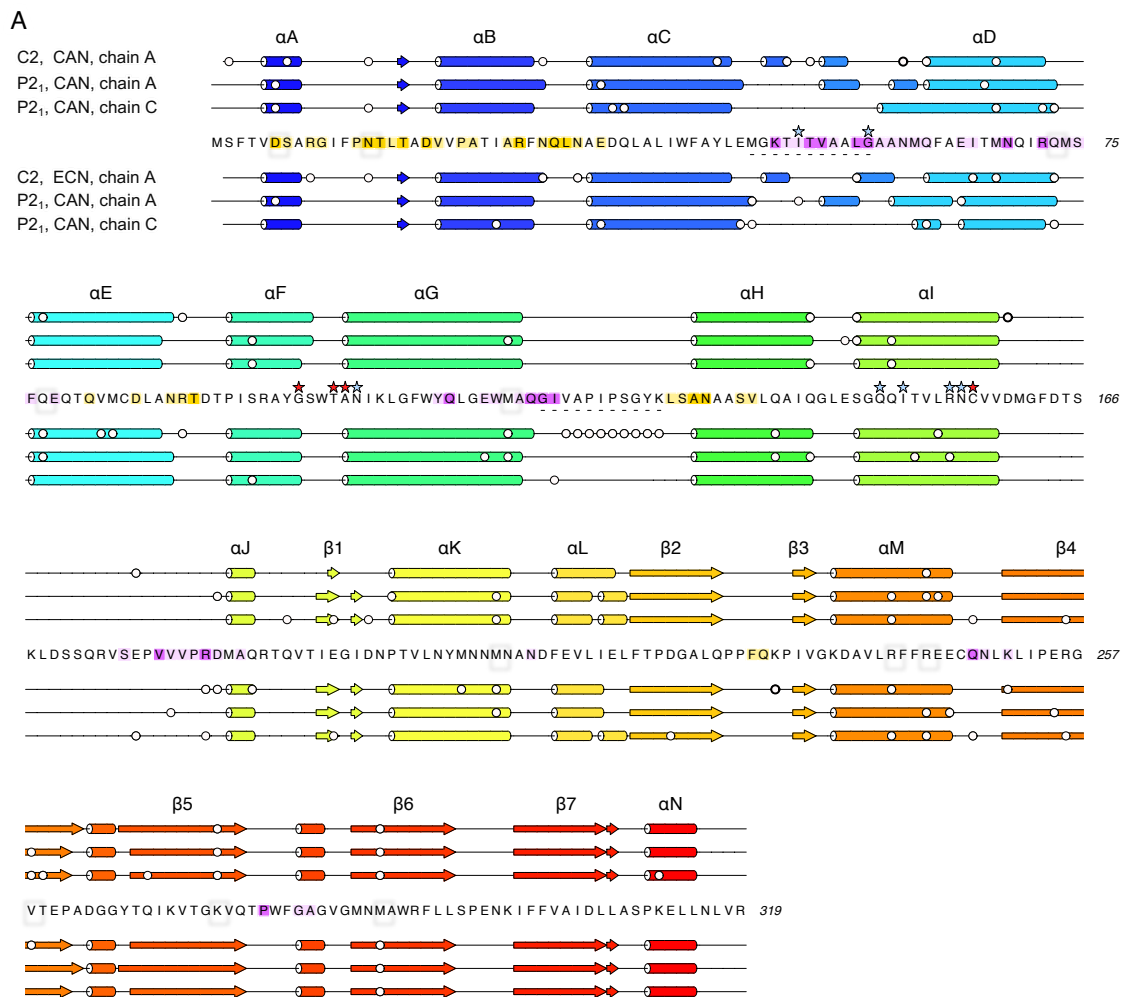
Figure 9. The naturally occurring OCP dimer is found in all OCP crystals, including those of Plankto-OCP. Residues involved in the dimerization are highlighted in yellow, whereas residues involved in the formation of interface X are highlighted in purple. Dark and light colouring indicate residues involved in polar and van der Walls interactions, respectively. Squares highlight residues present in alternate conformations in at least 50% of the analyzed Plankto-OCP chains. (A) The secondary structure of OCP is overall well conserved amongst Plankto-OCP structures obtained in different space groups and with different pigments. White dots highlight residues which are observed in alternate conformations. Blue stars indicate residues which have been shown to play a role in the OCP-PBS interaction, and red stars point to residues that could be at the origin of the stronger attachment of Plankto-OCP to the Syn-PBS. (B-C). The asymmetric unit of the $P2_1$ crystals features a dimer (here shown as a ribbon with the two facing monomers colored sequence-wise, from cold (N-ter) to hot (C-ter) colors), whereas in $C2$ crystals, the dimer is crystallographic, hence only a single monomer is found in the asymmetric unit. (D) Polar contacts at the dimerization interface involve a conserved salt-bridge between D19 and R27, as well as conserved H-bonds between facing D6 and T90, and between facing N134 and N14, T15, and T17. (E, F, G) The $C2$ structures display a more compact conformation than the $P2_1$ structures, at both the dimer (E, F) and at the monomer levels (G). The figure illustrates the trajectory followed by Plankto-OCP as we interpolate from the $C2$-CAN to the $P2_1$-CAN structure, highlighting the secondary structure elements which diverge most upon packing in the two crystal types. Arrows show the overall direction travelled by domains as we interpolate between the $C2$-Can and $P2_1$-CAN Plankto-OCP.
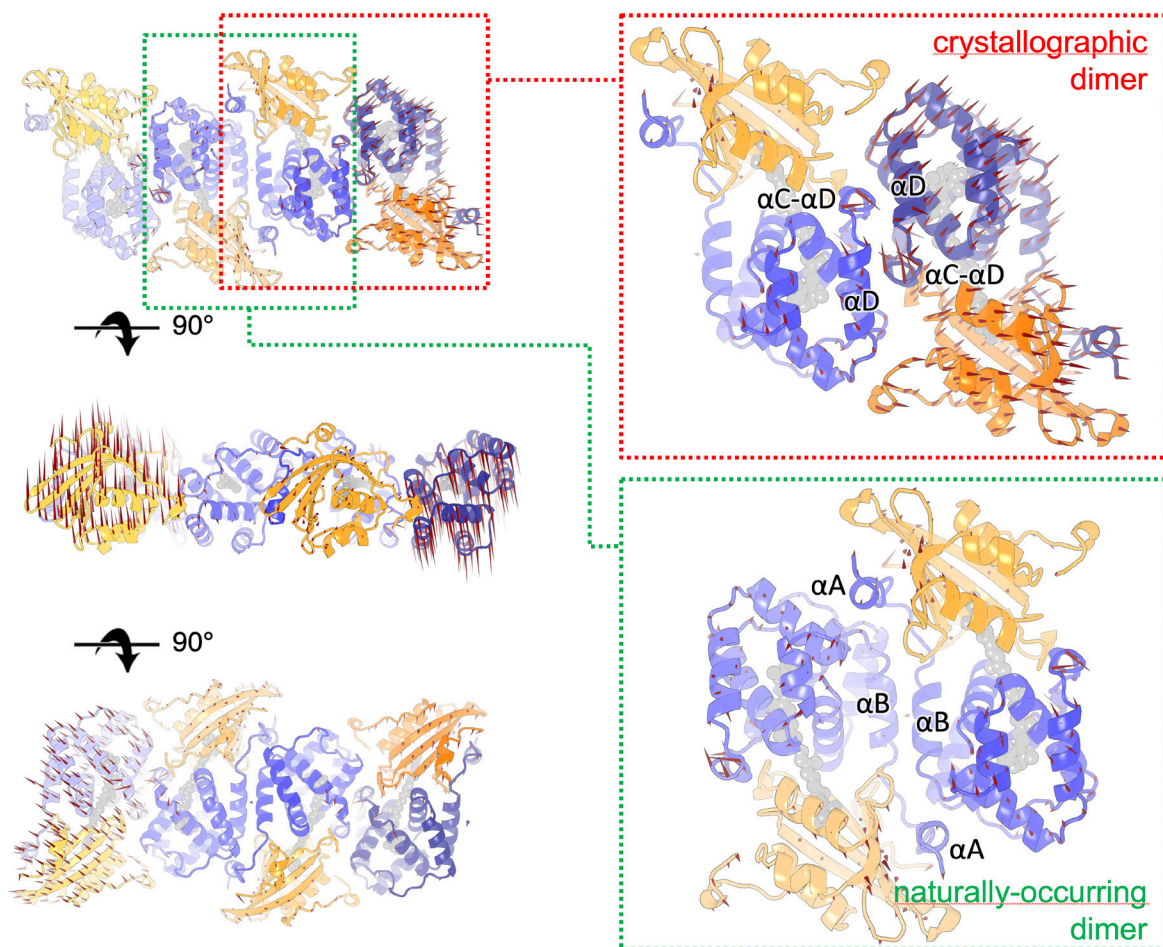

Figure 10: The *Planktothrix* OCP features two similarly large packing interfaces in crystals. In Plankto-OCP crystals, a large interface, additional to the dimerization interface (Table S1), is found which we coined interface X (Table S3). This interface, mainly contributed by by helices αD, αG and

αJ and by the αC-β4 and β5-β6 loops, matches the dimerization interface, in $P2_1$ crystals (BSA of ~1050 Å^2), but largely exceeds it, in the $C2$ crystals (BSA of ~1600 Å^2). Changes in the extent of interface X result in a reorientation of domains in each monomer forming the naturally-occurring dimer, and in an increase in the opening angle between monomers, in the dimer. Arrows indicate the direction and distance along which Cα atoms travel as we interpolate from the $P2_1$ to the $C2$ crystals.

Further analysis of the crystalline interfaces reveals that differences between the $P2_1$ and $C2$ crystals originate at a second large interface, absent in previously characterized OCP structures (Figure 10). This additional interface, coined interface X, corresponds to the dimerization interface in the $P2_1$ crystals (BSA of 1001.6 and 1054.6 Å^2 in the Ntag-Plankto-OCP$_{CAN}$ and Ntag-Plankto-OCP$_{ECN}$ structures, respectively) but largely exceeds it in the $C2$ crystals (BSA of 1650.3 and 1548.7 Å^2 in the Plankto-OCP$_{CAN}$ and Plankto-OCP$_{ECN}$ structures) (Supplementary Table S3). Interface X involves multiple secondary structure elements, including the αC-αD loop (~ 20 and 36 % of the overall BSA in $C2$ and $P2_1$ crystals, respectively), αD (~ 20 and 10 %, respectively), αE (~ 10 and 5 %, respectively), αG and the αG-αH loop (20 and 30 %, respectively), the linker (20 and 10 %), and the αM-β4 (~ 5 and 4 %, respectively) and β5-β6 (~ 2 and 5 %, respectively) loops (Supplementary Table S3). Only the first two structural elements contribute H-bonds at interface X in the $P2_1$ crystals, whereas all of them do in the $C2$ crystals (Supplementary Table S3). Conformational changes in αG and in the αC-αD and αG-αH loops, and resultantly changes in the BSA contributed by the αC-αD loop (+8 and +24 % in the Ntag-Plankto-OCP$_{CAN}$ and Ntag-Plankto-OCP$_{ECN}$ structures, respectively), αD (-64 and -68 %, respectively), αE (-70 and -66 %, respectively) and the linker (-74 and -68 %, respectively), explain the shrunken interface X in the $P2_1$ crystals, compared to the $C2$ crystals (Supplementary Table S3). These changes in packing translate to changes in the opening-angles at the dimerization (Figure 9E, F, G) and NTD/CTD interfaces (Figure 11), offering a glimpse into the molecular breathing motions that animate OCP, at both the monomer and the dimer levels (Figure 10). Briefly, monomers come closer to one another in the $P2_1$ (asymmetric unit) dimer than in the $C2$ (crystallographic) dimer (change in opening-angle and distance between chains: -5.6° and +1.1 Å for Ntag-Plankto-OCP$_{CAN}$; - 6.8° and + 1.2 Å for Ntag-Plankto-OCP$_{ECN}$).

The $P2_1$ monomers are nonetheless characterized by an increased opening angle between the NTD and the CTD (Figures 9G, 10 and 11). Chain A shows a larger deviation with respect to the unique chain in $C2$ crystals (change in opening-angle and distance between the NTD and CTD: +3.1° and +1.0 Å for Ntag-Plankto-OCP$_{CAN}$; +4.6° and +1.0 Å for Ntag-Plankto-OCP$_{ECN}$) than chain B (change in opening-angle and distance between the NTD and CTD: +1.3° and +0.4 Å for Ntag-Plankto-OCP$_{CAN}$; +1.4° and +0.3 Å for Ntag-Plankto-OCP$_{ECN}$) (Figure 9). As a result, the predicted radii of gyration (Rg) for the $P2_1$ asymmetric unit dimers (26.16

and 26.12 Å for Ntag-Plankto-OCP$_{CAN}$ and Ntag-Plankto-OCP$_{ECN}$, respectively) are larger than those predicted for the $C2$ crystallographic dimers (26.01 and 25.90 Å for Ntag-Plankto-OCP$_{CAN}$ and Ntag-Plankto-OCP$_{ECN}$, respectively) (Supplementary Table S2). Consistently, $P2_1$ chain B features a structure that is intermediate between $P2_1$ chain A and the unique C2 chain (change in opening-angle and distance between the NTD and CTD in $P2_1$ chain A with respect to $P2_1$ chain B: +3.3° and +0.9 Å for Ntag-Plankto-OCP$_{CAN}$; +4.0° and +0.7 Å for Ntag-Plankto-OCP$_{ECN}$) (Figure 11A). This is visible also in the predicted Rg for the various chains (20.81, 20.67 and 20.52 Å for Ntag- $P2_1$ chain A, $P2_1$ chain B and $C2$ Plankto-OCP$_{CAN}$, respectively; and 20.73, 20.50 and 20.48 Å for the Ntag-Plankto-OCP$_{ECN}$ counterparts, respectively) (Supplementary Table S2). Altogether, these changes affect the positioning of the carotenoid which, despite preservation of H-bonds from its carbonyl oxygen to Y203(OH) (2.5-2.8 Å distance between non-hydrogen atoms) and W290(NH1) (2.8-3.0 Å distance between non-hydrogen atoms) and a quasi-perfect alignment of its β1-ring in the CTD, tilts towards Y44 in the $P2_1$ structures (Figure 11B). With respect to the $C2$ Ntag-Plankto-OCP$_{CAN}$ structure, the tilt angles of the carotenoid are 3.8 and 1.8° in chains A and B of the $P2_1$ Ntag-Plankto-OCP$_{ECN}$ structure, 3.2 and 2.9° in chains A and B of the $P2_1$ Ntag-Plankto-OCP$_{CAN}$ structure, and 0.8° in the $C2$ Ntag-Plankto-OCP$_{ECN}$ structure. Thus, crystal packing traps different conformations of the Ntag-Plankto-OCP monomers, which differ (i) in the conformation displayed, at interface X, by αG and the αC-αD and αG-αH loops, (ii) in the opening angle between domains, at the NTD/CTD interface, (iii) in the opening angle between monomers, in the biological dimer; and (iv) in the positioning of the carotenoid (Figures 9-12). It is of important note that despite these changes, and the presence of two alternate side-chain conformations for R155 in the Ntag-Plankto-OCP$_{ECN}$ structures, the R155-E246 salt-bridge and N104-W279 H-bond, which support the NTD / CTD interface, are preserved in all structures (distance between non-hydrogen atoms 2.8-3.2 Å) (Supplementary Figures 4 and 5). We also note that previously determined structures of *Synechocystis*, *Anabaena*, *Tolypothrix* and *Arthrospira* OCP align best with the $C2$ Ntag-Plankto-OCP$_{CAN}$ and Ntag-Plankto-OCP$_{ECN}$, suggesting that these should be used for comparisons, rather than the $P2_1$ structures (Supplementary Table S2). In this context, it must be acknowledged that differences in the opening angle between the NTD and the CTD can also be seen from the comparison of the two chains constituting the asymmetric unit dimer in the *Anabaena* OCP structure (PDB id: 5hgr), with chain A aligning best with the $C2$ Ntag-Plankto-OCP conformers. We last note that ECN-functionalized OCP monomers and dimers are more compact than the CAN-functionalized counterparts (Figure 11 and Supplementary Table S2), and that a similar trend is visible in the comparison of CAN-functionalized (PDB id: 4xb5; one chain with a predicted radius of gyration of 20.49 Å) and ECN-functionalized (PDB id: 3mg1; two chains with predicted radii of gyration of 20.34 and

20.33 Å) NtagSyn-OCP structures. In the case of the Plankto-OCP structure, conformational changes again concentrate in the NTD (Figure 12).
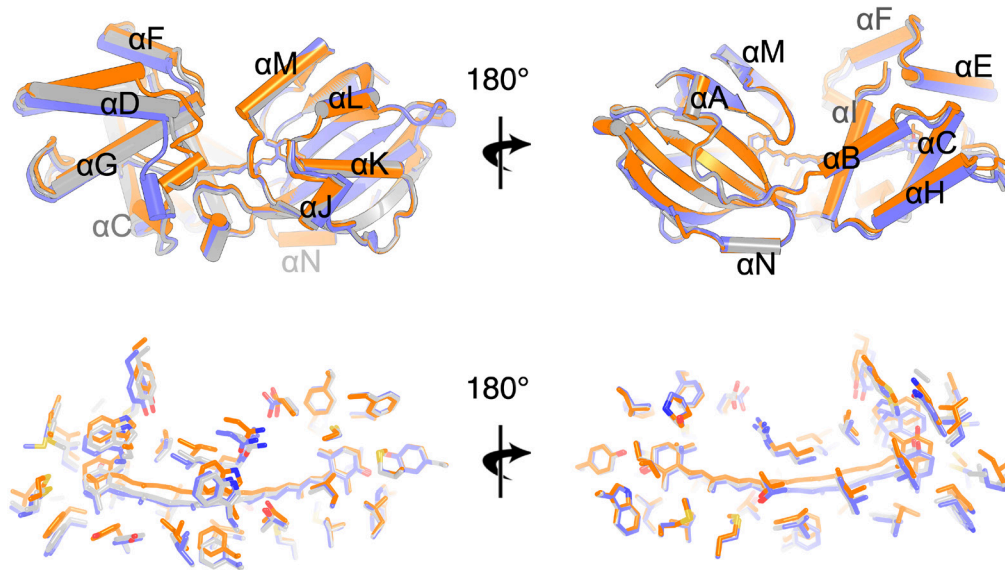

Figure 11: Plankto-OCP structures differ in the compaction of the monomer as well as in the internal structure of the NTD. (A) The *C*2 (orange), and *P*2$_1$ chain A (slate) and chain B (grey) are overlaid as ribbons. Structural alignment, performed using the CTD atoms, highlight the change in opening angle between the CTD and the NTD. Indeed, the CTD structure is highly conserved with hardly no conformational changes observed amongst structures. Large differences are yet seen in the NTD, notably in the αC-αD and αG-αH loops, but as well in the relative positioning of αC and αD helices. Here, the Plankto-OCP-CAN structures are shown, but the same observations were made when comparing the Plankto-OCP-ECN structures. (B) Close up view on CAN and on the residues lining the carotenoid tunnel. A change in the orientation of the carotenoid is seen upon compaction of the OCP structure due to change in space group.
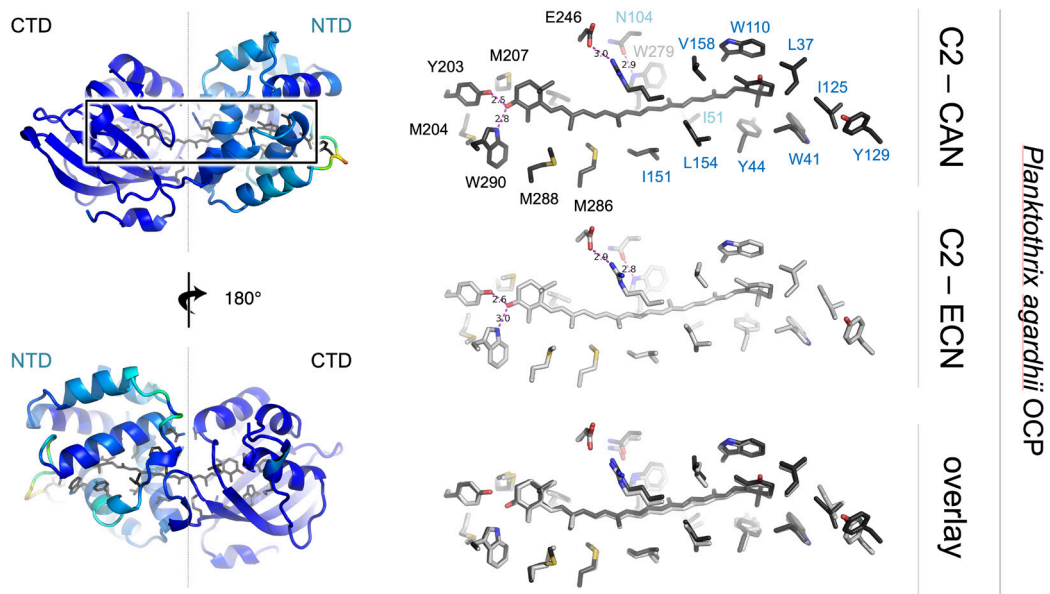

Figure 12: Conformational changes observed upon change of the functionalizing carotenoid are limited to the NTD. (A) The structure of Plankto-OCP-CAN is shown as a ribbon colored from

cold to hot colors as a function of the RMSD to the Plankto-OCP-ECN structure. (B) Close-up view on the carotenoid and residues lining the homonymous tunnel. The orientation in (B) is similar to that in the upper panel of (A).

Conformational changes at the Cα level are best visualized in Cα-Cα distance difference matrices (DDM). Calculated using the $C2$ Ntag-Plankto-OCP$_{CAN}$ structure as a reference, these confirm that the main difference between the $P2_1$ chain A, $P2_1$ chain B and $C2$ structures is a change in the orientation of the NTD vs. the CTD, accompanied (or triggered) by a change in the conformation of αA and the αC-αD and αG-αH loops. As a result, the two loops draw away from the CTD, pulling with them αC, αD, αE, αF and αG (Figure 13A). Conformational changes are far less pronounced in the CTD, where only β5 slightly changes position, moving away from αJ, β2 and αM (Figure 13A). In this context, it should be recalled that aside αA, the NTD consists of two 4-helix bundles contributed by helices αB-αC-αH-αI and αD-αE-αF-αG, respectively, which appose one onto the other leaving a central void that constitutes the carotenoid tunnel in the NTD. Our structural comparison indicates that regions most affected by the change in space group are those linking the two bundles, with conformational changes affecting the position – but not the internal structure – of the second bundle with respect to the CTD. Interestingly, the αC-αD and αG-αH loops are also the secondary structure elements most affected by the change in functionalizing carotenoid. It is visible from the comparison of the $C2$ structures, that these changes result in a modification of the distance between helices αD and αF, on the one hand, and the CTD, on the other hand. Thus, the structural dynamics at the basis of the change in space group and those resulting from the change in functionalizing carotenoid are localized in the same regions of the protein. This suggests that they could reflect a functional role. In line with this hypothesis, calculation of a DDM between the isolated NTD of Syn-OCP$_{CAN}$, considered as a surrogate for the structure of the NTD in OCP^R, and the NTD in the dark-adapted Syn-OCP$_{CAN}$^{O} reveals major changes in the αC-αD and αG-αH loops (Figure 13B), which result in a dramatic rearrangement of the first αB-αC-αH-αI bundle whilst leaving the internal conformation of the αD-αE-αF-αG bundle unperturbed. Thus, like changes in space group and functionalizing carotenoid in Ntag-Plankto-OCP, photoactivation affects the internal structure and relative positioning of the Syn-OCP αB-αC-αH-αI bundle through conformational changes in the αC-αD and αG-αH loops, while the second αD-αE-αF-αG bundle appears stable and acts as a base. This observation is surprising given that the interface between the first bundle and the CTD is larger (BSA of 643.2 Å^2; four H-bonds and a salt bridge) than that between the second bundle and the CTD (BSA of 189.3 Å^2; 1 H-bond). Regardless, our results show that the two most mobile regions across the NTD – and therefore, across the whole Plankto-OCP – are the αC-αD and αG-αH loops, making these the first candidates to explain the increased photoactivation efficiency of Plankto-OCP.
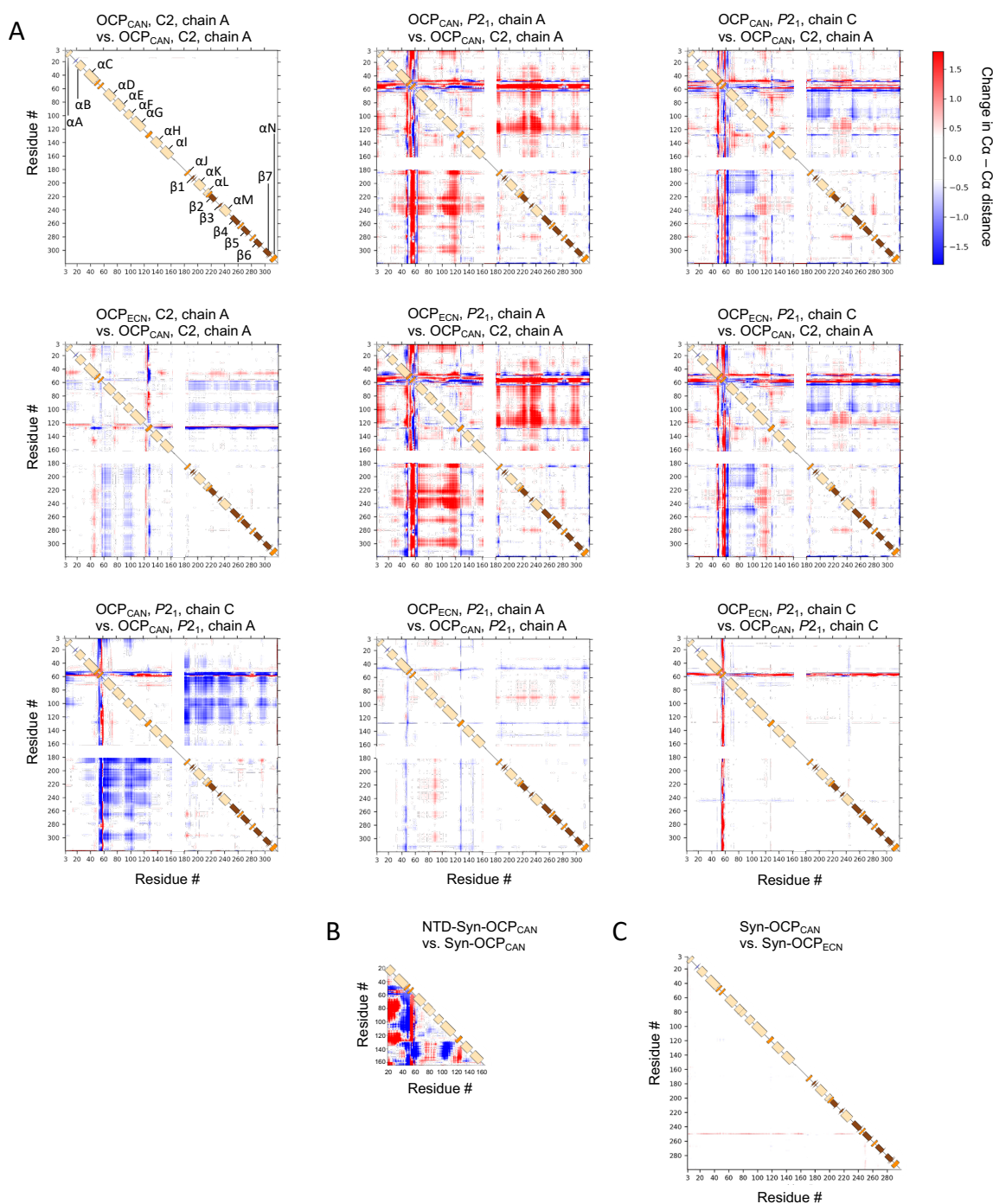
Figure 13: Crystal packing traps different conformations of the Ntag-Plankto-OCP monomers.
(A) Changes in Cα-Cα distances across in the various ECN- and CAN-functionalized *C*2 and *P*2$_1$ chains were monitored by computing Cα-Cα difference-distance matrices (DDM). As a reference structure, we used the *C*2 Plankto-OCP-CAN (2 first rows), or either chain A or C of the *P*2$_1$ PlanktoOCP-CAN structure (third line). In each DDM, the lower and upper panels (separated by a sketch of the secondary structure) show the changes in Cα-Cα distances for alternate conformers A and B with respect to the reference structure. Indeed, alternate conformations are seen in all Plankto-OCP structures. The overall similarity between upper and lower panels indicates that alternate conformations hardly affect the protein backbone. In the *P*2$_1$ crystals, two chains are found, which either display a more expanded (chain A) or a more compact (chain B) structure, due to changes in the opening angle between the NTD and the CTD. The DDM further indicates that these changes

33

stem from helix αD, and the αC-αD and αG-αH loops, either drawing away (chain A) or coming closer (chain B) to the CTD, respectively. Comparison of the *C*2-CAN and *C*2-ECN structures suggests that the presence of CAN results in a more compact protein. Support to this hypothesis could not be obtained from comparison of the *P*2$_1$ chain A or *P*2$_1$ chain B structures. Nonetheless, we observe a similar trend when comparing, either in the CAN-functionalized or the ECN-functionalized states, *P*2$_1$ chain C and *P*2$_1$ chain A. Thus, changes in functionalizing carotenoid have a lesser influence on the OCP conformation than changes in space group. (B) DDM calculated for the isolated NTD of Syn-OCP-CAN vs. Syn-OCP-CAN. This DDM suggests that upon photoactivation, large scale conformational changes occur in the NTD that mainly result in helix αB drawing away from helices αD to αG, while the αC-αD loop comes closer to these and to αH to αI. Also, αG edges closer to helices αH to αI, while the αG-αH loop draws farther. (C) DDM calculated for Syn-OCP$_{CAN}$ vs. Syn-OCP$_{ECN}$. Hardly no change in the Syn-OCP structure is seen upon change in the functionalizing carotenoid.

The αC-αD loop conformation differs in the *P*2$_1$ chain A, *P*2$_1$ chain B and *C*2 structures, but is overall preserved in each pair of ECN- and CAN-functionalized structures – notwithstanding the presence of multiple residues in alternate conformations in the C2 Ntag-Plankto-OCP$_{ECN}$ structure (Figure 11 and Supplementary Table S2). The αG-αH loop conformation is overall preserved among *P*2$_1$ structures, with only a slight displacement of αH observed between the *P*2$_1$ chains A and B, as a result of changes in the αC conformation concomitant to those in the αC-αD loop (Figures 11 and 13). The αG-αH loop conformation is yet more divergent among the *C*2 structures, with the *C*2 Ntag-Plankto-OCP$_{ECN}$ structure displaying two alternate main-chain conformations for the highly-conserved residues 122-VAPIPSGYKL-130, of which none overlaps with the conformations observed in *C*2 Ntag-Plankto-OCP$_{CAN}$ and in the *P*2$_1$ chains (Supplementary Figure 6 and Supplementary Table S2). Interestingly, these changes in the conformations of the αC-αD and αG-αH loops result in the opening/closing of water-channels from the protein surface to the carotenoid tunnel in the NTD. Briefly, four main channels (#1, #2, #3 and #4) can be identified on the basis of our structures (Supplementary Figures 7, 8 and 9). The first one (#1), which is colinear with the carotenoid axis and adjacent to the β2-ring, features the fully conserved L37, M83, M117 and I125 (Supplementary Figures 7, 8 and 9) at its bottleneck and encompasses the binding site of the carotenoid in the structure of the isolated NTD of Syn-OCP$_{CAN}$ (Supplementary Tables S2 and S4). Channel #1 is opened in all Ntag-Plankto-OCP structures, and as well in all previously determined OCP structures. In the *C*2 Ntag-Plankto-OCP$_{ECN}$ structure, however, the presence of two alternate main-chain conformations for αG-αH loop residues 120-GIAPIPSGYKL-131 (Supplementary Figure S6) results in two configurations of the channel (see Supplementary Table S4) characterized by either a wider or narrower opening (Supplementary Figures 6, 8 and 9). The enlargement of channel #1 is compulsory for the carotenoid to translocate fully across the NTD, as illustrated by the observation that the αG-αH loop displays a large change in conformation in the structure of the isolated NTD of Syn-OCP$_{CAN}$, compared to the NTD in dark-adapted Syn-OCP^O$_{CAN}$ (Figure 13B) [21]. Hence the two *C*2 Ntag-Plankto-OCP$_{ECN}$ conformers offer an illustration of

how structural dynamics in the αG-αH loop may participate in the regulation of photoactivation. We yet note that none of the conformations observed in our various Ntag-Plankto-OCP structures, or in the previously determined OCP structures, matches that found in the structure of the isolated NTD of Syn-OCP$_{CAN}$.

The second (#2), third (#3) and fourth channel (#4) are all perpendicular to the carotenoid tunnel, and open on either side of Y44 side chain, ending up just above the β2-ring of the carotenoid (#2) or its second terpene unit (#3, #4) (Supplementary Figures 7 and 8). Channel #2 features W41 and Y44 at its bottleneck, whereas channel #3 is lined by Y44, M47, I51, I151 and F280, and channel #4 by Y44, Y111 and αG (Supplementary Figures 7 and 8). Residues W41, M47, I151 and M280 are strictly conserved, whereas V53 and I53 fill the structural position of Plankto-OCP I51 in Ana-OCP and Syn-OCP, respectively, and Y44 and Y111 are replaced by a phenylalanine (F44) and an asparagine (N111), respectively, in Ana-OCP. We find that channel #2 is opened toward the bulk in all $P2_1$ structures, albeit a much wider opening is observed in chain A of the $P2_1$ Ntag-Plankto-OCP$_{ECN}$ structure, due to a large swing of Y44 towards Y111 (Supplementary Figure 8) – *i.e.* away from W41. Of note, Y44 is found in alternate side-chain conformations in the *C*2 Ntag-Plankto-OCP$_{CAN}$ structure, and as well in the previously determined Syn-OCP$_{ECN}$ structure (Supplementary Figure 8). Additionally, channel #3 is opened in chain A of the $P2_1$ Ntag-Plankto-OCP$_{CAN}$ and Ntag-Plankto-OCP$_{ECN}$ structures, although in only one alternate conformer due to alternate conformations in M47. In both *C*2 structures, channel #2 and #3 are closed. Nonetheless, in one of the two alternate conformers of the C2 Ntag-Plankto-OCP$_{CAN}$ structure, channel #4 is opened (Supplementary Figure 7). We note that all previously determined OCP structures feature similar openings of the carotenoid tunnel towards the bulk that are perpendicular to the carotenoid axis. For example, channels #3 and #4 are opened in the Syn-OCP structures (PDB ids: 3mg1 and 4xb5), while channels #2 and channel #3 are opened in the *Tolypothrix* OCP structure (PDB id: 6pq1) and in the two chains of the asymmetric unit dimer from the *Arthrospira* structure (PDB id: 5ui2; also referred to as *Limnospira*). In *Tolypothrix* OCP, a supplementary channel (#5) is observed, ~ 180° apart from channel #2, which is lined by the highly conserved F28, I40, S157 and M161 (Supplementary Figure 10). The opening of channel #5, which alike channel #2 ends up above the β2-ring of the carotenoid albeit from the other side of the tunnel, mainly depends on the side chain conformation of M161 in the *Tolypothrix* OCP structure. Channel #5 is also opened in the two chains of the asymmetric unit dimer from the *Anabaena* OCP structure (PDB id: 5hgr), where its opening if facilitated by the substitution of I40 (in Plankto-OCP, Syn-OCP, *Arthrospira* and *Tolypothrix* OCPs) for a valine – atop the conformational change in M161. Channel #3 is additionally opened in chain B of Ana-OCP, but closed in chain A due to change in the conformation of M47. Thus, the Ntag-Plankto-OCP

structures illustrate that the opening of channel #1-4 mainly depends on the conformations displayed by residues in αC (A33-E46) and in the αC-αD (M47-G57) and αG-αH (G120-L131) loops. The *Tolypothrix* and *Anabaena* OCP structures additionally reveal the existence of another channel (#5), which ends up on the side of the carotenoid β2 ring where the methyl or carbonyl oxygen atom of ECN and CAN are exposed, respectively. Given that the *Tolypothrix* OCP features the same residue distribution as Plankto-OCP, Syn-OCP and *Arthrospira* OCP along the five channels, it is possible that channel #5 would open in these as well.

We noted earlier that the positioning of the carotenoid differs in the various Ntag-Plankto-OCP structures, due to changes in the opening angle between domains, *i.e.* at the NTD/CTD interface. Besides this point, the most notable dissimilarity in the carotenoid tunnel is the presence of a methionine at position 207, instead of a leucine in other OCPs (L205 in Syn-OCP, and L207 in *Anabaena, Arthrospira* and *Tolypothrix* OCP) (Supplementary Figures 5, 6, 10). At position 288, a methionine is found in Plankto-OCP, Ana-OCP (PDB id: 5hgr) and *Tolypothrix* (PDB id: 6pq1)) OCP (PDB id: 4xb5), which is substituted for by an isoleucine in *Synechocystis* (I286) and *Arthrospira* OCP (I288) (Supplementary Figures 5, 6, 10). Thus, Plankto-OCP is particularly enriched in methionine residues. Of these two substitutions, we speculate that the one which may be related to the higher photoactivation rate of OCP is the former, since the slower *Tolypothrix* and *Anabaena* OCP also feature a methionine at position 288. Conversely, only Plankto-OCP features a methionine at position 207. The only other structural difference between the carotenoid tunnels of Plankto-OCP and Syn-OCP is the placement of Plankto-OCP I51 at the position occupied by Syn-OCP I53, due to changes in the sequence of the αC-αD loop (47-MGKT**ITV**AA**L**GAA-59 in Plankto-OCP vs. 47-MGKT**L**T**I**AA**P**GAA-59 in Syn-OCP) which adopts the same conformation in Syn-OCP, Ana-OCP, Arthro-OCP and Toply-OCP structures, but exhibits varying conformations in the various Ntag-Plankto-OCP structures (Supplementary Figures 10 and 12). Given that the αC-αD loop in Ana-OCP (47-MGKT**ITV**AA**P**GAA-59) differs from that in Plankto-OCP only by the substitution of L56 for a proline – found as well in Syn-OCP, Arthro-OCP and Toply-OCP – it is reasonable to assign the increased dynamics of this loop in Plankto-OCP to this residue. P56 indeed fits into a groove at the surface of the NTD (formed by S60, M61, G108, Y111 and W277 in Syn-OCP; S60, M61, G108, N111 and W279 in Ana-OCP; and N60, M61, G108, Y111 and W279 in Arthro-OCP and Toply-OCP), whereas it is solvent exposed in Plankto-OCP (Supplementary Figure 10).

36

Discussion

Here, we report results from a comparative analysis of OCP1 functional properties across different cyanobacterial species, including the previously uncharacterized Plankto-OCP and the most studied Syn-OCP. All OCP-related functional properties – photoactivation, thermal recovery, interaction of the OCP^R state with the PBS and consequential fluorescence quenching – were examined for their dependence on the functionalizing carotenoid (ECN vs. CAN). We also investigated the influence of His-tagging at either the N or C-terminus, which afforded information on the role of the NTE (αA) and the CTT (αN) in the various molecular processes. In an attempt to rationalize functional observations on the basis of structural differences, we solved the *hitherto* uncharacterized structures of Plankto-OCP in the ECN- and CAN-functionalized states, each in two space groups, and compared them to the available structures of ECN- and CAN-functionalized Syn-OCP [17, 21]. When useful, we also included in our structural comparison the structures of CAN-functionalized *Anabaena* OCP [58], hECN-functionalized *Arthrospira* OCP [8] and of CAN-functionalized *Tolypothrix* OCP [30].

Initially, our interest in Plankto-OCP was sparked by the recent observation that the *in vivo* OCP-related NPQ-mechanism is more efficient in *Planktothrix* than in *Synechocystis* cells [37]. The functional characterization of Plankto-OCP properties revealed the molecular basis for this phenotype, showing that it not only photoactivates faster than Syn-OCP, but also recovers faster (especially at 9°C). Such a fast thermal recovery had thus far been observed only for OCP2 and OCPX variants, but not for members of the OCP1 clade. Indeed, *Synechocystis*, *Arthrospira* and *Tolypothrix* OCP1 are all characterized by a slow recovery at 9°C. Similar to these, the recovery of Plankto-OCP can be further accelerated by addition of FRP, confirming its appartenance to the OCP1 clade. In previous studies, it was found that slow recovery and the ability to bind to FRP coincide in the OCP1 clade, as opposed to OCP2 and OCPX [16] which recover faster thermally but are unable to bind FRP. Based on sequence alignments, it was further suggested that the defining feature of the OCP1 clade is the presence of residues R229 and D262 (*Synechocystis* number), which are absent in OCP2 and OCPX [16]. Our data confirm that presence of R229 and D262 correlates with the ability to bind FRP, but indicate that the slow recovery rate of *Synechocystis*, *Arthrospira* and *Tolypothrix* OCP1 is unrelated to their presence.

The faster photoactivation and recovery of Plankto-OCP could stem from its higher protein flexibility, illustrated by the large structural diversity amongst Plankto-OCP crystalline structures. Indeed, crystal packing traps different conformations of the Ntag-Plankto-OCP monomers, which differ (i) in the conformation displayed by αG and the αC-αD and αG-αH loops, (ii) in the opening angle between domains, at the NTD/CTD interface, (iii) in the opening

37

angle between monomers, in the naturally-occurring dark-adapted dimer; and (iv) in the positioning of the carotenoid (Figures 9-13). The Plankto-OCP structures offer a peek into the molecular breathing motions that animate OCP, at the monomer and the dimer levels. The $P2_1$ structures demonstrate that the two monomers in a dimer can adopt slightly different structures, differing in the opening angle at the NTD/CTD interface, and consequently, in the orientation of the carotenoid in the tunnel. These differences could account for the repeated observations that two types of OCP coexist in darkness in spectroscopic experiments [40]. The conformations present in the $C2$ structures match best those displayed by chain B in the $P2_1$ structures. Nonetheless, they are not strictly equivalent, differing not only in the opening angle at the NTD/CTD interface, but as well in the exact positioning of helices around the carotenoid and in the conformation displayed by the αC-αD and αG-αH loops. These two loops indeed show the highest diversity among the various structures reported herein, whereas they adopt the same conformation in Syn-OCP, Ana-OCP, Arthro-OCP and Tolypo-OCP structures.

The $P2_1$ chain A and $P2_1$ chain B structures feature a "porous wall", traversed by channels perpendicular to the carotenoid tunnel, whereas the $C2$ structures feature a carotenoid tunnel that is insulated from the bulk, except at its extremities (Supplementary Figures 7, 8 and 9, and Supplementary Tables S2 and S4). Together, the six chains illustrate that the opening of channels #1-4 mainly depends on the conformations displayed by residues in αC (A33-E46; channels 1-2) and in the αC-αD (M47-G57; channels 2-4) and αG-αH (G120-L131; channel 1) loops, and question the possible role of water access to the carotenoid tunnel in the photoactivation mechanism – and/or its limitation. The enlargement of channel #1 is compulsory for the carotenoid to translocate fully across the NTD, and accordingly, the αG-αH loop displays a large change in conformation in the isolated NTD of Syn-OCP$_{CAN}$, as compared to the NTD in dark-adapted Syn-OCP$^O_{CAN}$ [21] (Figure 13). Two alternate conformations are observed for this loop in the $C2$ Ntag-Plankto-OCP$_{ECN}$ structure, which offer an illustration of how structural dynamics could participate in the regulation of photoactivation. We yet note that none of the conformations observed in our various Ntag-Plankto-OCP structures, or in the previously determined OCP structures, matches that found in the structure of the isolated NTD of Syn-OCP$_{CAN}$ [21]. We also investigated if the presence of multiple alternate conformations could underlie the higher photoactivity of Plankto-OCP. Plotting these against the secondary (Figure 9A and Supplementary Table S2) or tertiary structure, we identify the αC-αD (M47-G57) loop, αM and β4 as clusters, *i.e.* secondary-structure elements or epitopes more prone to alternate conformations irrespective of the space group or functionalizing carotenoid (Figure 9A). W288, at the CTD end of the carotenoid tunnel, is present in alternate conformations in all structures. Additionally, D6, N14, Q73, Q77, M117, M207, R241, R244, V258, K275 are present in alternate conformations in at three out of the six Plankto-OCP chains analyzed. In

conclusion, we propose that the structural traits which explain the higher photoactivation rate of Plankto-OCP are the increased flexibility in the αC-αD (M47-G57) and αG-αH (G120-L131) loops, which results in opening of water channels to the carotenoid tunnel, and increased molecular breathing motions at the levels of the dimer, the NTD/CTD interface, and the NTD helix core. As to the increased recovery rate, we hypothesize that it originates from a decreased stabilization of the Plankto-OCP^R state. Hence, we first compared residues distribution along the carotenoid tunnel in the NTD. The only structural difference between the NTD tunnels of Plankto-OCP and Syn-OCP is the placement of Plankto-OCP I51 at the position occupied by Syn-OCP I53, due to changes in the sequence of the αC-αD loop (47-MGKT**ITV**AA**L**GAA-59 in Plankto-OCP *vs.* 47-MGKT**L**T**I**AA**P**GAA-59 in Syn-OCP) (Supplementary Figures 5, 6 and 10). Another, more hypothetical means by which the Plankto-OCP^R state would be rendered less stable could be through a decrease in the affinity of the CTT for the empty CTD tunnel. Syn-OCP is unique among the variants discussed herein in that it features a 314-NFAR-317 sequence at its C-terminus instead of 316-NLVR-319 in the other OCP (Supplementary Figure 10). The combined substitution of a leucine for phenylalanine, and of a valine for alanine, could account for a higher affinity of the Syn-OCP CTT for the empty CTD tunnel. Reversely, the presence in Plankto-OCP of a methionine at position 288, (Planktothrix numeration) instead of an isoleucine at position 286 in Syn-OCP, could decrease the affinity of the Plankto-OCP CTT for the empty CTD tunnel.

We also further examined the effect of His-tagging at the N- or C-terminus on the various functional properties of OCP (Figures 3 and 8). Indeed, both the NTE and the CTT have been proposed to play important roles in the OCP photoactivation and recovery mechanisms. We found that irrespectively of the variant, the N-tagged protein displays the best match to the native protein, both in terms of photoactivation rate and thermal recovery rate. Native Syn-OCP and Plankto-OCP display the fastest photoactivation profile, indicating that increased disorder in their NTE or a weaker interaction between the NTE and CTD does not benefit photoactivation as was previously suggested [61]. Recovery was also found to be faster in native Syn-OCP and Plankto-OCP than in their His-tagged counterparts. A dramatic drop in the recovery rate was notably observed for the C-tagged Plankto-OCP, which could stem either from a higher stability of the OCP^R state in presence of a C-terminal His-tag or from a frustrated recovery of the OCP^O state due to hindered rebinding of the CTT to the CTD β-sheet. Regardless, these results point to an important role played by the CTT in the OCP^R to OCP^O recovery. Little is known regarding the configuration of the CTT residues in the OCP^R state and its role in OCP photoactivation and recovery. However, it was shown that in the *Synechocystis* C-terminal domain homologue (CTDH), which belongs to a family of carotenoid-transporting proteins homologous to the OCP CTD [35, 36], the CTT can exchange between

a closed conformation, whereby it covers the empty carotenoid tunnel, and an opened conformation, similar to that observed in OCP^O. By analogy, it was proposed that one of the last steps of OCP photoactivation is the repositioning of the CTT on the empty CTD-half of the carotenoid tunnel. Presence of a six-histidine tag in the CTT could hinder this movement, leading to slower kinetics of photoactivation and recovery. In conclusion, our results suggest that re-binding to the CTD β-sheet of the CTT, and to a lower extent of the NTE, are rate limiting steps in the thermal recovery of the OCP^O state, and that completion of these steps is inhibited by presence of a His-tag at their C or N-terminal extremities, respectively.

The position of the His-tag also influences the PBS quenching, with again a more pronounced effect of His-tagging at the C-terminus than at the N-terminus of OCP. In the past, we proposed that the presence of a six-histidine tag upstream the NTE could destabilize the interaction with the PBS [61], yet the present data invalidate the hypothesis, demonstrating that N-tagged and native OCP detach as swiftly from the PBS. Contrastingly, introduction of the six-histidine tag downstream the CTT results in increased PBS-fluorescence quenching and slower fluorescence recovery. This result can be rationalized by envisioning that the C-terminal his-tag strongly stabilizes the PBS-bound OCP^R structure, possibly through interaction of the tag with PBS amino acids. A cross-species characterization of OCP/PBS complexes allowed the discovery that irrespective of His-tagging, Plankto-OCP binds stronger to Syn-PBS than Syn-OCP. Furthermore, Plankto-OCP binds stronger to Syn-PBS than to Plankto-PBS, echoing the previous observation that *Arthrospira* and *Anabaena* OCPs bind stronger to Syn-PBS than to *Arthrospira* and *Anabaena* PBS, respectively [42]. Recent studies on Syn-OCP have shown that besides R155, early demonstrated as compulsory for the OCP/PBS interaction [62], residues L51, P56, G57, A58, N104, I151, and N156 play important roles in the interaction [63]. Recall that in all OCP, N104 and R155 are involved in the stabilization of the OCP^O state by contributing H-bonds to the NTD/CTD interface (N104(OD1) to W277(Syn)/W279 (Plankto)(NE1); R155(NH2) to E244 (Syn)/E246 (Plankto)(OE1)). In addition, in all structures but the Plankto-OCP structures, N104 contributes to the stabilization of the linker by establishing a H-bond to E174(OE1). As G57, N104, I151, R155 and N156 are structurally conserved in Plankto-OCP, one can eliminate the hypothesis that the observed differences in Syn-PBS quenching would stem from these. As to Syn-OCP L51, it is replaced by an isoleucine in the *Anabaena*, *Limnospira* and *Tolypothrix* proteins, nonetheless the side chain occupies the same position in all structures, fitting in a groove contributed by M47, I151, F280 and V284, at the NTD-CTD interface. In Plankto-OCP, this residue is conserved; however, due to changes in the sequence of the αC-αD loop (47-MGKT**ITV**AA**L**GAA-59 in Plankto-OCP vs. 47-MGKT**L**TIAA**P**GAA-59 in Syn-OCP), Plankto-OCP L51 is found at the position occupied by I53 in all previously-determined OCP structures. Syn-OCP P56 is replaced by a leucine in Plankto-

OCP, but it is conserved in other OCPs. Hence, the difference in PBS binding-affinity and fluorescence-quenching observed between Syn-OCP and Plankto-OCP could stem from changes in the sequence and structure of the αC-αD loop. Within 4 Å of R155, supposedly central to the interaction, we find four additional candidate positions at which residue substitutions could explain the higher affinity of Plankto-OCP as compared to Syn-OCP: G99, T102, A103 and C157, respectively. These residues are substituted by A99, S102, P103 and A157 in Syn-OCP, and by A99, S102, P103 and S157 in Ana-OCP. Future mutagenesis work concentrated on these results could unveil the molecular basis for this unexpected cross-species preference for the Syn-PBS. Specific to the lower affinity of Plankto-OCP for Plankto-PBS than Syn-PBS, it must be recalled that OCP binding to the PBS is very sensitive to the structural intactness of the PBS core. Although 77K fluorescence spectra of both isolated PBS suggested a perfect energy transfer from PC to the last core emitters, we cannot discard the hypothesis that a slightly different interaction between the APC trimers could be at the origin of the weaker OCP-PBS binding observed for *Arthrospira* and *Planktothrix* species-specific complexes. It was also observed that the Plankto-Lcm protein is more sensitive to proteolysis than Syn-Lcm (Supplementary Figure 3). Hence the reduced affinity of Plankto-OCP for the Plankto-PBS could originate in the partial degradation of the Lcm component.

We last examined the influence of the functionalizing carotenoid on OCP excited and intermediate states dynamics. Indeed, irrespective of the species, CAN-functionalized OCP photoactivates faster and recovers slower than ECN-functionalized OCP. Using fs-ns and ns-s transient absorption spectroscopy on ECN- and CAN-functionalized Plankto-OCP and Syn-OCP, we inquired the time scale(s) on which the gain in photoactivation efficiency occurs for the CAN-functionalized proteins. We observed differences in the respective yields of the S_1, ICT and S* states, but nearly no change in their characteristic lifetimes nor in the P_1 yield (Table 1). Hence, the difference in photoactivation rate of ECN- and CAN-functionalized OCP does not stem from changes in their excited state dynamics nor in the P1 formation quantum yield. Furthermore, the increased S* yield observed for CAN-functionalized Plankto-OCP and Syn-OCP is not mirrored by an increase in the P_1 yield, suggesting that the former is not its only precursor. Clear differences between the four tested OCPs were yet observed in the ns-s time scale. First, we observed for Plankto-OCP a larger drop in difference absorption at 563 nm on the ns-μs time scale, which could sign for a sub-optimal translocation of ECN and CAN into the Plankto-NTD, as compared to the Syn-NTD. This hypothesis is supported by the observation that ECN-functionalized OCP forms more compact monomers and dimers, wherein migration of the carotenoid could be facilitated (Figures 12 and 13). Regardless, the most striking differences between Plankto-OCP and Syn-OCP are visible in the ns-ms time window, while those between CAN- and ECN-functionalized OCP concentrate in the ms-s

timescale. Thus, our results suggest that both carotenoid translocation and NTE/CTT detachments are affected by the change in protein scaffold, whereas it is domain dissociation that is most affected by a change in the functionalizing carotenoid. Our data support that domain dissociation is faster and more efficient in CAN-functionalized OCPs, with no decline observed in the difference absorption at 550 nm. Specific to Plankto-OCP$_{CAN}$, a faster domain separation is observed with virtually no recovery to OCP^O on the µs-s timescale (100% efficiency from P_3 to final OCP^R). The increased photoactivation rate of Plankto-CAN is likely grounded in this property. Thus, the differences observed in the photoactivation speed of CAN- and ECN-functionalized Plankto-OCP and Syn-OCP stem from changes in the (comparatively-slow) carotenoid translocation, NTE/CTT detachment and domain dissociation steps – rather than from not changes in the excited-state dynamics or P1 formation quantum yield.

It remains unclear whether or not canthaxanthin can be generally used as a functionalizing carotenoid for OCP in the natural context. When expressed in their parent strain, *Arthrospira* and *Synechocystis* OCPs [8, 11] bind hECN, while *Tolypothrix* OCP1 binds CAN [30]. Recombinant expression of *Arthrospira* and *Anabaena* OCPs in *Synechocystis* cells also yield an hECN-functionalized proteins [32, 42]. Yet, when overexpressed and isolated from CAN-producing *E. coli* cells, all these OCPs bind CAN, suggesting that OCPs may alternatively bind hECN or CAN depending on the carotenoid presents in the cells. We earlier reported the partial inability of *Anabaena* and *Tolypothrix* OCP to fully convert to OCP^R, when functionalized by ECN [8, 11]. Here, thermal recovery kinetics were found to be slower in the CAN-functionalized Syn- and Plankto-OCPs, possibly due to a reduced stabilization of the OCP^R state by ECN, as compared to CAN. Assuming that the β-rings of the carotenoid are exposed to the bulk in the OCP^R state, as suggested by the structure of the CAN-functionalized isolated NTD of Syn-OCP (PDB id: 4xb4; [21]), the higher stability of the CAN-functionalized OCP^R could result from the presence of an oxygen on its β2 ring, favoring interaction with the bulk. A similar stability would thus be expected for hECN, which features a hydroxyl group in the β2-ring. Hence, the possibility remains that all OCPs bind hECN in their parent strain. Supporting this hypothesis is the observation that quenching by *Plankto*-OCP of the *Plankto*-PBS fluorescence is efficient only when ECN is used as the functionalizing carotenoid (or when the protein is tagged at the C-terminus). This result incidentally suggests that in the *Planktothrix* cells, the carotenoid functionalizing OCP is not CAN.

It is difficult to rationalize the observation that CAN-OCP interaction with the PBS is weaker than that with ECN-OCP (Figures 7 and 8, and Supplementary Figure 11). These results are at variance with the observation that CAN stabilizes the OCP^R state, and suggest that the isolated OCP^R and PBS-bound-OCP^R structures could differ. The sole difference between

CAN- and ECN-functionalized OCP^R is the presence of a carbonyl oxygen on the β2-ring, but this difference should not affect binding to the PBS, since its epitope has been mapped at the opposite end of the carotenoid tunnel in the NTD, proximate to R155. Thus, it is presumably the β1-ring, identical in CAN and ECN, which will be in contact with the PBS. A possible explanation could be that upon OCP binding to PBS, the carotenoid migrates into to the PBS, enabling a better interaction with the bilin pigments, as proposed earlier [21, 64]. If it is the β1-ring that plunges into the PBS – *i.e.,* the carotenoid moves backwards with respect to the OCP^O to OCP^R transition – then the β2-ring will be repositioned inside the highly hydrophobic carotenoid tunnel, possibly past its original position in the OCP^O structure, which would explain the reduced stability of the CAN-functionalized OCP-PBS complexes, due to replacement of a methyl in ECN by a carbonyl oxygen in CAN. Thus, our results support the hypothesis that the isolated and PBS-bound OCP^R differ. If true, OCP-related quenching of PBS-fluorescence would be a two-step reaction (at the very least), with first the binding of OCP^R to PBS, and then a change in the OCP^R structure – as initially proposed by [21, 64].

Conclusion:

We here have reported on a comparative structure-function study on two OCPs from the OCP1 clade, *i.e.,* Syn-OCP and Plankto-OCP. Our results suggest that Plankto-OCP is more flexible and we speculate that this increase in flexibility explains its faster photoactivation and recovery. Specifically, our Plankto-OCP structures evidence increased structural dynamics in the αC-αD loop, which was shown to have a central role in the interaction between OCP^R and PBS [62-64]. Increased dynamics in this loop could be at the origin of the stronger binding of Plankto-OCP (compared to Syn-OCP) to Syn-PBS. Irrespectively, our data point to more efficient carotenoid translocation and NTE/CTT detachments in Plankto-OCP. We also show that presence of a His-tag influences both the photocycle of OCP (see also Nizinski et al., submitted; doi.org/10.1101/2021.12.26.474187) and its interaction with the PBS. Most impacting is introduction of the tag at the C-terminus, which results in both large damping of the photoactivation and recovery and in stronger binding to the PBS, suggesting an important role for the CTT in these molecular processes, The CTT has been proposed to shift from open position in OCP^O (in which the CTT interacts with the CTD) to a close position in OCP^R (in which the CTT presumably binds in the carotenoid tunnel); our results are also suggestive of an involvement of the CTT in PBS binding. Our work last uncovers the strong influence of the nature of the functionalizing carotenoid on all aspects of OCP function. The mere substitution on ring β2 of a dimethyl in ECN by a carbonyl in CAN results in increased photoactivation efficiency, which our ns-s spectroscopic data suggest to be due to faster domain dissociation. Nonetheless, CAN-functionalized OCP display reduced recovery, reduced binding to PBS and reduced energy-quenching activity. These features could result from thwarted back-migration of CAN, compared to ECN, as required for recovery and, presumably, PBS quenching and stabilization of the OCP-PBS complex.

Table 1: Lifetime, time constants and quantum yields obtained from femtosecond and nanosecond transient absorption experiments. (A) Lifetimes of ICT/S_1/S*/P_1 states derived from femtosecond transient absorption measurements (from data in Figure 5 and Figure S2), and estimated formation quantum yields derived from preexponential factors at 490 nm (the magnitude of the bleaching band of each DAS was extracted from the fitting procedure; for more details, see the Materials and Methods section and Nizinski et al., submitted; doi.org/10.1101/2021.12.26.474187). The standard error is 10%. P_1 yields are corrected for its positive absorbance contribution at 500 nm. (B) Time constants and yields (percentages in brackets) derived from ns-s transient absorption measurements for P_1, P_2/$P_{2'}$ and P_3/P_{N-M-X}. Only in the case of P_1 are the value in brackets actual quantum yields; for P_2/$P_{2'}$ and P_3/P_{N-M-X}, they rather indicate the relative contribution of the corresponding exponential terms to the overall decay and growing components (indicated in bold). Percentages in the OCP^R column are formation quantum yields of the red absorbing intermediates remaining at 10 ms (determined by a comparative actinometry method with ruthenium complex; for details, see Material and Methods section and [45]).

Table 1A	ICT	S_1	S*	P_1
Syn-OCP$_{CAN}$	0.50 ps (25 %)	3.2 ps (59 %)	7.6 ps (16 %)	> 1 ns (0.4 %)
Syn-OCP$_{ECN}$	0.66 ps (36 %)	2.8 ps (56 %)	10.1 ps (8 %)	> 1 ns (0.6 %)
Plankto-OCP$_{CAN}$	0.43 ps (28 %)	2.8 ps (56 %)	7.1 ps (16 %)	> 1 ns (0.4 %)
Plankto-OCP$_{ECN}$	0.30 ps (44 %)	1.7 ps (40 %)	5.4 ps (16 %)	> 1 ns (0.4 %)

Table 1B	P_1	P_2 / $P_{2'}$	P_3 / P_{N-M-X}	OCP^R
Syn-OCP$_{CAN}$	45 ns (60 %)	830 ns (15 %) 22 µs (6 %)	380 µs (19 %)	0.11 %
Syn-OCP$_{ECN}$	46 ns (48 %)	400 ns (14 %)	890 µs (22 %) 83 ms (16 %)	0.08 %
Plankto-OCP$_{CAN}$	52 ns (65 %)	1.3 µs (35 %)	**1.1 ms (33 %)** **24 ms (67 %)**	0.17 %
Plankto-OCP$_{ECN}$	41 ns (35 %)	410 ns (31 %) 1.9 µs (19 %)	3.0 ms (15 %)	0.05 %

Table 2. Data collection and refinement statistics. Statistics for the highest-resolution shell are shown in parentheses**.**

	C2_100K_ECN	C2_100K_CAN	P21_100K_ECN	P21_100K_CAN
PDB id.	7QD0	7QCZ	7QD1	7QD2
Wavelength	0.95	1.54	0.98	0.99
Resolution range	32.44 - 1.7 (1.76 - 1.7)	18.26 - 1.85 (1.92 - 1.85)	75.58 - 1.71 (1.75 - 1.71)	43.6 - 1.4 (1.45 - 1.4)
Space group	*C* 1 2 1	*C* 1 2 1	*P* 1 2_1 1	*P* 1 2_1 1
Unit cell	81.4 64.87 61.69 90 117.911 90	82.01 67.5 61.94 90 117.821 90	63.36 65.90 77.37 90 102.354 90	63.46 65.94 77.28 90 102.262 90
Total reflections	100512 (10488)	57189 (4493)	214925 (6579)	272526 (27565)
Unique reflections	30920 (3104)	23822 (1963)	60669 (2735)	115206 (11285)
Multiplicity	3.3 (3.4)	2.4 (2.3)	3.5 (2.4)	2.4 (2.4)
Completeness (%)	98.61 (99.42)	92.59 (76.47)	90.0 (54.8)	93.90 (92.54)
Mean I/sigma(I)	13.78 (1.84)	11.96 (1.81)	11.16 (1.21)	11.47 (1.90)
Wilson B-factor	25.57	26.48	27.75	21.13
R-merge	0.046 (0.6095)	0.052 (0.5806)	0.063 (0.685)	0.036 (0.3938)
R-meas	0.055 (0.7256)	0.066 (0.7384)	0.074 (0.877)	0.046 (0.5066)
R-pim	0.030 (0.3894)	0.040 (0.4513)	0.038 (0.547)	0.028 (0.3153)
CC1/2	0.999 (0.843)	0.997 (0.682)	0.997 (0.426)	0.998 (0.852)
Reflections used in refinement	30858 (3097)	23803 (1963)	60658 (1519)	115047 (11285)
Reflections used for R-free	1545 (154)	1190 (98)	3015 (81)	5753 (564)
R-work	0.1785 (0.3045)	0.1761 (0.3740)	0.1806 (0.4771)	0.2002 (0.2804)
R-free	0.2231 (0.3397)	0.2450 (0.4107)	0.2159 (0.5757)	0.2309 (0.2942)
CC(work)	0.967 (0.901)	0.968 (0.771)	0.942 (0.671)	0.956 (0.626)
CC(free)	0.957 (0.811)	0.937 (0.709)	0.923 (0.470)	0.942 (0.563)
Number of non-hydrogen atoms	3042	3017	5885	5819
macromolecules	2698	2542	5099	5120
ligands	85	42	82	100
solvent	259	433	704	599
Protein residues	308	309	621	614
RMS(bonds)	0.030	0.005	0.05	0.007
RMS(angles)	1.44	0.86	1.34	0.94
Ramachandran favored (%)	98.36	97.70	98.86	98.68
Ramachandran allowed (%)	0.66	1.64	0.98	0.99
Ramachandran outliers (%)	0.99	0.66	0.16	0.33
Rotamer outliers (%)	3.44	2.91	2.76	2.18
Molprobity score	1.84	1.79	1.72	1.51
Clashscore	7.46	6.65	5.68	5.02
Average B-factor	34.30	30.31	32.37	30.40
macromolecules	32.93	28.56	31.03	29.61
ligands	37.47	23.55	24.54	24.16
solvent	47.50	41.26	43.00	38.15

References:

[1] N. Adir, H. Zer, S. Shochat, I. Ohad, Photoinhibition - a historical perspective, Photosynth Res, 76 (2003) 343-370.

[2] A. Krieger-Liszkay, Singlet oxygen production in photosynthesis, Journal of Experimental Botany, 56 (2005) 337-346.

[3] K.K. Niyogi, T.B. Truong, Evolution of flexible non-photochemical quenching mechanisms that regulate light harvesting in oxygenic photosynthesis, Current opinion in plant biology, 16 (2013) 307-314.

[4] D. Kirilovsky, C.A. Kerfeld, The orange carotenoid protein in photoprotection of photosystem II in cyanobacteria, Biochim Biophys Acta, 1817 (2012) 158-166.

[5] D. Kirilovsky, C.A. Kerfeld, Cyanobacterial photoprotection by the orange carotenoid protein, Nature plants, 2 (2016) 16180.

[6] F. Muzzopappa, D. Kirilovsky, Changing Color for Photoprotection: The Orange Carotenoid Protein, Trends Plant Sci, (2019).

[7] A. Wilson, G. Ajlani, J.M. Verbavatz, I. Vass, C.A. Kerfeld, D. Kirilovsky, A soluble carotenoid protein involved in phycobilisome-related energy dissipation in cyanobacteria, Plant Cell, 18 (2006) 992-1007.

[8] C.A. Kerfeld, M.R. Sawaya, V. Brahmandam, D. Cascio, K.K. Ho, C.C. Trevithick-Sutton, D.W. Krogmann, T.O. Yeates, The crystal structure of a cyanobacterial water-soluble carotenoid binding protein, Structure, 11 (2003) 55-65.

[9] A. Sedoud, R. Lopez-Igual, A. Ur Rehman, A. Wilson, F. Perreau, C. Boulay, I. Vass, A. Krieger-Liszkay, D. Kirilovsky, The Cyanobacterial Photoactive Orange Carotenoid Protein Is an Excellent Singlet Oxygen Quencher, Plant Cell, 26 (2014) 1781-1791.

[10] M. Gwizdala, A. Wilson, D. Kirilovsky, *In vitro* reconstitution of the cyanobacterial photoprotective mechanism mediated by the Orange Carotenoid Protein in *Synechocystis* PCC 6803, Plant Cell, 23 (2011) 2631-2643.

[11] A. Wilson, C. Punginelli, A. Gall, C. Bonetti, M. Alexandre, J.M. Routaboul, C.A. Kerfeld, R. van Grondelle, B. Robert, J.T. Kennis, D. Kirilovsky, A photoactive carotenoid protein acting as light intensity sensor, Proc. Natl. Acad. Sci. U. S. A., 105 (2008) 12075-12080.

[12] E.G. Maksimov, N.N. Sluchanko, Y.B. Slonimskiy, E.A. Slutskaya, A.V. Stepanov, A.M. Argentova-Stevens, E.A. Shirshin, G.V. Tsoraev, K.E. Klementiev, O.V. Slatinskaya, E.P. Lukashev, T. Friedrich, V.Z. Paschenko, A.B. Rubin, The photocycle of orange carotenoid protein conceals distinct intermediates and asynchronous changes in the carotenoid and protein components, Scientific reports, 7 (2017) 15548.

[13] M.Y. Gorbunov, F.I. Kuzminov, V.V. Fadeev, J.D. Kim, P.G. Falkowski, A kinetic model of non-photochemical quenching in cyanobacteria, Biochim Biophys Acta, 1807 (2011) 1591-1599.

[14] H. Bao, M.R. Melnicki, E.G. Pawlowski, M. Sutter, M. Agostoni, S. Lechno-Yossef, F. Cai, B.L. Montgomery, C.A. Kerfeld, Additional families of orange carotenoid proteins in the photoprotective system of cyanobacteria, Nature plants, 3 (2017) 17089.

[15] S. Lechno-Yossef, M.R. Melnicki, H. Bao, B.L. Montgomery, C.A. Kerfeld, Synthetic OCP heterodimers are photoactive and recapitulate the fusion of two primitive carotenoproteins in the evolution of cyanobacterial photoprotection, Plant J, 91 (2017) 646-656.

[16] F. Muzzopappa, A. Wilson, D. Kirilovsky, Interdomain interactions reveal the molecular evolution of the orange carotenoid protein, Nature plants, 5 (2019) 1076-1086.

[17] A. Wilson, J.N. Kinney, P.H. Zwart, C. Punginelli, S. D'Haene, F. Perreau, M.G. Klein, D. Kirilovsky, C.A. Kerfeld, Structural determinants underlying photoprotection in the photoactive orange carotenoid protein of cyanobacteria, J Biol Chem, 285 (2010) 18364-18375.

[18] S. Gupta, M. Sutter, S.G. Remesh, M.A. Dominguez-Martin, H. Bao, X.A. Feng, L.G. Chan, C.J. Petzold, C.A. Kerfeld, C.Y. Ralston, X-ray radiolytic labeling reveals the molecular basis of orange carotenoid protein photoprotection and its interactions with fluorescence recovery protein, J Biol Chem, 294 (2019) 8848-8860.

[19] P.E. Konold, I.H.M. van Stokkum, F. Muzzopappa, A. Wilson, M.L. Groot, D. Kirilovsky, J.T.M. Kennis, Photoactivation Mechanism, Timing of Protein Secondary Structure Dynamics and Carotenoid Translocation in the Orange Carotenoid Protein, Journal of the American Chemical Society, 141 (2019) 520-530.

[20] Y.B. Slonimskiy, E.G. Maksimov, E.P. Lukashev, M. Moldenhauer, T. Friedrich, N.N. Sluchanko, Engineering the photoactive orange carotenoid protein with redox-controllable structural dynamics and photoprotective function, Biochimica et biophysica acta. Bioenergetics, 1861 (2020) 148174.

[21] R.L. Leverenz, M. Sutter, A. Wilson, S. Gupta, A. Thurotte, C. Bourcier de Carbon, C.J. Petzold, C. Ralston, F. Perreau, D. Kirilovsky, C.A. Kerfeld, PHOTOSYNTHESIS. A 12 A carotenoid translocation in a photoswitch associated with cyanobacterial photoprotection, Science, 348 (2015) 1463-1466.

[22] M. Bondanza, L. Cupellini, P. Faccioli, B. Mennucci, Molecular Mechanisms of Activation in the Orange Carotenoid Protein Revealed by Molecular Dynamics, Journal of the American Chemical Society, 142 (2020) 21829-21841.

[23] E.G. Maksimov, E.A. Protasova, G.V. Tsoraev, I.A. Yaroshevich, A.I. Maydykovskiy, E.A. Shirshin, T.S. Gostev, A. Jelzow, M. Moldenhauer, Y.B. Slonimskiy, N.N. Sluchanko, T. Friedrich, Probing of carotenoid-tryptophan hydrogen bonding dynamics in the single-tryptophan photoactive Orange Carotenoid Protein, Scientific reports, 10 (2020) 11729.

[24] N.B. Pigni, K.L. Clark, W.F. Beck, J.A. Gascon, Spectral Signatures of Canthaxanthin Translocation in the Orange Carotenoid Protein, The journal of physical chemistry, 124 (2020) 11387-11395.

[25] R. Berera, I.H. van Stokkum, S. d'Haene, J.T. Kennis, R. van Grondelle, J.P. Dekker, A mechanism of energy dissipation in cyanobacteria, Biophysical journal, 96 (2009) 2261-2267.

[26] R. Berera, I.H. van Stokkum, M. Gwizdala, A. Wilson, D. Kirilovsky, R. van Grondelle, The photophysics of the orange carotenoid protein, a light-powered molecular switch, The journal of physical chemistry, 116 (2012) 2568-2574.

[27] P.O. Andersson, T. Gillbro, Photophysics and dynamics of the lowest excited singlet state in long substituted polyenes with implications to the very longchain limit, J. Chem. Phys, 103 (1995) 2509-2519.

[28] C.C. Gradinaru, J.T. Kennis, E. Papagiannakis, I.H. van Stokkum, R.J. Cogdell, G.R. Fleming, R.A. Niederman, R. van Grondelle, An unusual pathway of excitation energy deactivation in carotenoids: singlet-to-triplet conversion on an ultrafast timescale in a photosynthetic antenna, Proc Natl Acad Sci U S A, 98 (2001) 2364-2369.

[29] V. Balevicius, Jr., D. Abramavicius, T. Polivka, A. Galestian Pour, J. Hauer, A Unified Picture of S* in Carotenoids, The journal of physical chemistry letters, 7 (2016) 3347-3352.

[30] V. Kuznetsova, M.A. Dominguez-Martin, H. Bao, S. Gupta, M. Sutter, M. Kloz, M. Rebarz, M. Precek, Y. Chen, C.J. Petzold, C.Y. Ralston, C.A. Kerfeld, T. Polivka, Comparative ultrafast spectroscopy and structural analysis of OCP1 and OCP2 from Tolypothrix, Biochimica et biophysica acta. Bioenergetics, 1861 (2020) 148120.

[31] T. Lenzer, F. Ehlers, M. Scholz, R. Oswald, K. Oum, Assignment of carotene S* state features to the vibrationally hot ground electronic state, Phys Chem Chem Phys, 12 (2010) 8832-8839.

[32] C. Bourcier de Carbon, A. Thurotte, A. Wilson, F. Perreau, D. Kirilovsky, Biosynthesis of soluble carotenoid holoproteins in Escherichia coli, Scientific reports, 5 (2015) 9085.

[33] S. Gupta, M. Guttman, R.L. Leverenz, K. Zhumadilova, E.G. Pawlowski, C.J. Petzold, K.K. Lee, C.Y. Ralston, C.A. Kerfeld, Local and global structural drivers for the photoactivation of the orange carotenoid protein, Proc Natl Acad Sci U S A, 112 (2015) E5567-5574.

[34] A. Mezzetti, M. Alexandre, A. Thurotte, A. Wilson, M. Gwizdala, D. Kirilovsky, Two-Step Structural Changes in Orange Carotenoid Protein Photoactivation Revealed by Time-Resolved Fourier Transform Infrared Spectroscopy, The journal of physical chemistry, 123 (2019) 3259-3266.

[35] D. Harris, F. Muzzopappa, F. Glaser, A. Wilson, D. Kirilovsky, N. Adir, Structural dynamics in the C terminal domain homolog of orange carotenoid Protein reveals residues critical for carotenoid uptake, Biochimica et biophysica acta. Bioenergetics, 1861 (2020) 148214.

[36] D. Harris, A. Wilson, F. Muzzopappa, N.N. Sluchanko, T. Friedrich, E.G. Maksimov, D. Kirilovsky, N. Adir, Structural rearrangements in the C-terminal domain homolog of Orange Carotenoid Protein are crucial for carotenoid transfer, Communications Biology, 1 (2018) 125.

[37] C. Djediat, K. Feilke, A. Brochard, L. Caramelle, S. Kim Tiam, P. Setif, T. Gauvrit, C. Yepremian, A. Wilson, L. Talbot, B. Marie, D. Kirilovsky, C. Bernard, Light stress in green and red Planktothrix strains: The orange carotenoid protein and its related photoprotective mechanism, Biochimica et biophysica acta. Bioenergetics, 1861 (2020) 148037.

[38] A. Wilson, C. Punginelli, M. Couturier, F. Perrau, D. Kirilovsky, Essential role of two tyrosines and two tryptophans on photoprotection activity of the Orange Carotenoid Protein, Biochim Biophys Acta, 1807 (2011) 293-301.

[39] C. Punginelli, A. Wilson, J.M. Routaboul, D. Kirilovsky, Influence of zeaxanthin and echinenone binding on the activity of the Orange Carotenoid Protein, Biochim Biophys Acta, 1787 (2009) 280-288.

[40] V. Slouf, V. Kuznetsova, M. Fuciman, C.B. de Carbon, A. Wilson, D. Kirilovsky, T. Polivka, Ultrafast spectroscopy tracks carotenoid configurations in the orange and red carotenoid proteins from cyanobacteria, Photosynth Res, 131 (2017) 105-117.

[41] N.N. Sluchanko, K.E. Klementiev, E.A. Shirshin, G.V. Tsoraev, T. Friedrich, E.G. Maksimov, The purple Trp288Ala mutant of Synechocystis OCP persistently quenches phycobilisome fluorescence and tightly interacts with FRP, Biochim Biophys Acta, 1858 (2017) 1-11.

[42] D. Jallet, A. Thurotte, R.L. Leverenz, F. Perreau, C.A. Kerfeld, D. Kirilovsky, Specificity of the cyanobacterial orange carotenoid protein: influences of orange carotenoid protein and phycobilisome structures, Plant Physiol, 164 (2014) 790-804.

[43] Y. Kashino, H. Koike, K. Satoh, An improved sodium dodecyl sulfate-polyacrylamide gel electrophoresis system for the analysis of membrane protein complexes, Electrophoresis, 22 (2001) 1004-1007.

[44] G. Burdzinski, M. Bayda, G.L. Hug, M. Majchrzak, B. Marciniec, B. Marciniak, Time-resolved studies on the photoisomerization of a phenylene–silylene–vinylene type compound in its first singlet excited state, Journal of Luminescence, 131 (2011) 577-580.

[45] P. Muller, K. Brettel, [Ru(bpy)(3)](2+) as a reference in transient absorption spectroscopy: differential absorption coefficients for formation of the long-lived (3)MLCT excited state, Photochem Photobiol Sci, 11 (2012) 632-636.

[46] W. Kabsch, Xds, Acta Crystallogr D Biol Crystallogr, 66 (2010) 125-132.

[47] W. Kabsch, Integration, scaling, space-group assignment and post-refinement, Acta Crystallogr D Biol Crystallogr, 66 (2010) 133-144.

[48] A.J. McCoy, R.W. Grosse-Kunstleve, P.D. Adams, M.D. Winn, L.C. Storoni, R.J. Read, Phaser crystallographic software, Journal of applied crystallography, 40 (2007) 658-674.

[49] M.D. Winn, C.C. Ballard, K.D. Cowtan, E.J. Dodson, P. Emsley, P.R. Evans, R.M. Keegan, E.B. Krissinel, A.G. Leslie, A. McCoy, S.J. McNicholas, G.N. Murshudov, N.S. Pannu, E.A. Potterton, H.R. Powell, R.J. Read, A. Vagin, K.S. Wilson, Overview of the CCP4 suite and current developments, Acta Crystallogr D Biol Crystallogr, 67 (2011) 235-242.

[50] K. Cowtan, Fitting molecular fragments into electron density, Acta Crystallogr D Biol Crystallogr, 64 (2008) 83-89.

[51] K. Cowtan, Recent developments in classical density modification, Acta Crystallogr D Biol Crystallogr, 66 (2010) 470-478.

[52] G.N. Murshudov, P. Skubak, A.A. Lebedev, N.S. Pannu, R.A. Steiner, R.A. Nicholls, M.D. Winn, F. Long, A.A. Vagin, REFMAC5 for the refinement of macromolecular crystal structures, Acta Crystallogr D Biol Crystallogr, 67 (2011) 355-367.

[53] P. Emsley, B. Lohkamp, W.G. Scott, K. Cowtan, Features and development of Coot, Acta Crystallogr D Biol Crystallogr, 66 (2010) 486-501.

[54] W. Wriggers, K. Schulten, Protein domain movements: detection of rigid domains and visualization of hinges in comparisons of atomic coordinates, Proteins, 29 (1997) 1-14.

[55] E. Chovancova, A. Pavelka, P. Benes, O. Strnad, J. Brezovsky, B. Kozlikova, A. Gora, V. Sustr, M. Klvana, P. Medek, L. Biedermannova, J. Sochor, J. Damborsky, CAVER 3.0: a tool for the analysis of transport pathways in dynamic protein structures, PLoS computational biology, 8 (2012) e1002708.

[56] A.A. Arteni, G. Ajlani, E.J. Boekema, Structural organisation of phycobilisomes from *Synechocystis* sp. strain PCC6803 and their interaction with the membrane, Biochim Biophys Acta, 1787 (2009) 272-279.

[57] S. Bandara, Z. Ren, L. Lu, X. Zeng, H. Shin, K.H. Zhao, X. Yang, Photoactivation mechanism of a carotenoid-based photoreceptor, Proc Natl Acad Sci U S A, 114 (2017) 6286-6291.

[58] R. Lopez-Igual, A. Wilson, R.L. Leverenz, M.R. Melnicki, C. Bourcier de Carbon, M. Sutter, A. Turmo, F. Perreau, C.A. Kerfeld, D. Kirilovsky, Different Functions of the Paralogs to the N-Terminal Domain of the Orange Carotenoid Protein in the Cyanobacterium Anabaena sp. PCC 7120, Plant Physiol, 171 (2016) 1852-1866.

[59] I.A. Yaroshevich, E.G. Maksimov, N.N. Sluchanko, D.V. Zlenko, A.V. Stepanov, E.A. Slutskaya, Y.B. Slonimskiy, V.S. Botnarevskii, A. Remeeva, I. Gushchin, K. Kovalev, V.I. Gordeliy, I.V. Shelaev, F.E. Gostev, D. Khakhulin, V.V. Poddubnyy, T.S. Gostev, D.A. Cherepanov, T. Polivka, M. Kloz, T. Friedrich, V.Z. Paschenko, V.A. Nadtochenko, A.B. Rubin, M.P. Kirpichnikov, Role of hydrogen bond alternation and charge transfer states in photoactivation of the Orange Carotenoid Protein, Commun Biol, 4 (2021) 539.

[60] M. Golub, M. Moldenhauer, F.J. Schmitt, A. Feoktystov, H. Mandar, E. Maksimov, T. Friedrich, J. Pieper, Solution Structure and Conformational Flexibility in the Active State of the Orange Carotenoid Protein: Part I. Small-Angle Scattering, The journal of physical chemistry, 123 (2019) 9525-9535.

[61] A. Thurotte, R. Lopez-Igual, A. Wilson, L. Comolet, C. Bourcier de Carbon, F. Xiao, D. Kirilovsky, Regulation of Orange Carotenoid Protein Activity in Cyanobacterial Photoprotection, Plant Physiol, 169 (2015) 737-747.

[62] A. Wilson, M. Gwizdala, A. Mezzetti, M. Alexandre, C.A. Kerfeld, D. Kirilovsky, The essential role of the N-terminal domain of the orange carotenoid protein in cyanobacterial photoprotection: importance of a positive charge for phycobilisome binding, Plant Cell, 24 (2012) 1972-1983.

[63] A. Wilson, F. Muzzopappa, D. Kirilovsky, Elucidation of the essential amino acids involved in the binding of the cyanobacterial Orange Carotenoid Protein to the phycobilisome, Biochimica et biophysica acta. Bioenergetics, 1863 (2022) 148504.

[64] W. Lou, D.M. Niedzwiedzki, R.J. Jiang, R.E. Blankenship, H. Liu, Binding of red form of Orange Carotenoid Protein (OCP) to phycobilisome is not sufficient for quenching, Biochimica et biophysica acta. Bioenergetics, 1861 (2020) 148155.

Competing interests: Authors declare no competing interests.

Data and materials availability: Atomic coordinates and structure factors have been deposited in the Protein Data Bank under the following accession codes: 7qd0, 7qcZ, 7qd1 and 7qd2. All other data are available in the main text or the supplementary materials.

Figures captions:

Figure 1: Formation of OCP^R is a multi-step reaction that spans 12 decades in time. The figure which presents a working model for OCP photoactivation, summarizes findings from multiple studies [12, 19, 23]. The wavelength of maximum difference-absorbance (after subtraction of the OCP^O signal) is indicated for all intermediate states characterized to date. The P$_1$, P$_2$, P$_{2'}$ and P$_3$ were observed by Konold et al. 2019 in transient absorption UV-Vis experiments upon excitation at 470 nm of Ntag-Syn-OCP$_{ECN}$ [19]. Of important note, P$_{2'}$ was only observed in transient IR experiments, suggesting that it is characterized by a conformational change in the protein scaffold that does not influence the carotenoid electronic properties. P$_N$/P$_M$ and P$_X$ were observed by Maksimov et al. in time-resolved fluorimetry experiments upon excitation at 262 nm of the ECN-functionalized OCP-3FH mutant (W41F, W101F, W110F and W277H) featuring a single tryptophan at position W288 [23].

Figure 2: Photoactivation and recovery of native (non-tagged) CAN-functionalized *Synechocystis* and *Planktothrix* OCPs. (A and D) Absorbance spectra of Syn-OCP$_{CAN}$ (A) and Plankto-OCP$_{CAN}$ (D) at different times of illumination. (B and E) Differential absorbance spectra derived from A and D respectively. (C and F) Differential absorbance spectra normalized at 470 nm derived from A and D. (G-I) Kinetics of photoactivation (G) and recovery (H-I) of CAN-functionalized Syn-OCP (black) and Plankto-OCP (red). Inset in G: First 30 s of illumination. In (I), the effect of the presence of FRP is shown. The ratio FRP to OCP was 1:1. The accumulation of OCP^R and its thermal deactivation were followed by increase and decrease of absorbance at 550 nm. The OCPs were illuminated with white light (5 000 µmol photons m^{-2}. s^{-1}) at 9.5°C. Error bars: standard deviation. Each curve represents the mean of three independent measurements, respectively.

Figure 3: Presence of a His-tag has an impact on photoactivation and recovery. Effect of presence and position of His-tag on photoactivation (A-B) and recovery (C-D) of CAN-functionalized *Synechocystis* and *Planktothrix* OCPs. The accumulation of OCP^R and its thermal deactivation were followed by increase and decrease of absorbance at 550 nm. The OCPs were illuminated with white light (5 000 µmol photons m^{-2}. s^{-1}) at 9.5°C. Error bars: standard deviation. Each curve represents the mean of three independent measurements.

Figure 4: Effect of the nature of the functionalizing ketocarotenoid on photoactivation and recovery of N-terminus His-tagged *Synechocystis* and *Planktothrix* OCPs. (A-B) Kinetics of photoactivation of Syn-OCPs (A) and Plankto-OCPs (B) functionalized with ECN (red) or CAN (black). Inset in A and B: First 30 s of illumination. The OCPs were illuminated with white light (5 000 µmol photons m^{-2}. s^{-1}) at 9.5°C. (C and D) Thermal recovery of OCP^R in darkness of Syn-OCPs (C) and Plankto-OCPs (D) functionalized with ECN (red) or CAN (black). The accumulation of OCP^R and its thermal recovery were followed by increase and decrease of absorbance at 550 n, respectively. Error bars: standard deviation. Each curve represents the mean of three independent measurements, respectively (E and H) Absorbance spectra of ECN-Syn (E) and ECN-Plankto OCPs (H) at different times of illumination. (F and I) Raw difference absorbance spectra derived from E and H respectively. (G and J) Difference absorbance spectra derived from E and H, respectively, after normalization on the 470 nm band.

Figure 5: Femtosecond transient absorption data collected on the Ntag-Plankto-OCP. (A, B) Transient absorption spectra measured after excitation at 532 nm are shown for time

delays ranging between 0.14 and 1 ns for (A) Ntag-Plankto-OCP$_{ECN}$ and (B) Ntag-Plankto-OCP$_{CAN}$. All datasets were normalized to -1 at bleaching minimum, in both spectral and temporal dimensions. (C, D) Decay Associated Spectra (DAS) obtained from the global fit of the transient absorption data spectra shown in (A) and (B), respectively. Data were fitted using four exponential components convolved by a Gaussian pulse (IRF, 110 fs FWHM) and an offset (long-lived photo-product > 10 ns).

Figure 6: Nanosecond-second dynamics in CAN- and ECN-functionalized Plankto-OCP and Syn-OCP. Time evolution (50 ns to 1 s) of the difference absorption signals at 550 nm recorded on Plankto-OCP$_{ECN}$ (yellow), Plankto-OCP$_{CAN}$ (red), Syn-OCP$_{ECN}$ (green) and Syn-OCP$_{CAN}$ (blue) after excitation by a 532 nm ns-pulse. The intermediate states proposed [12, 19, 23] to underlie the observed absorption changes are indicated at the top of the figure. Measurements were carried out at 22°.

Figure 7: Effect of ketocarotenoid on OCP-PBS interaction. (A, C) *Synechocystis* (A) and *Planktothrix* (C) PBS fluorescence quenching induced at 23°C in 0.5 M phosphate buffer by CAN (black) and ECN (red) functionalized *Synechocystis* (A) and *Planktothrix* (C) native (non-tagged) OCPs. The OCP was pre-photoactivated by illumination with a strong white light (5 000 μmol photons m^{-2}. s^{-1}) at 4°C. The ratio OCP:PBS was 40:1. (B, D) Dark recovery of fluorescence in *Synechocystis* (B) and *Planktothrix* (D) phycobilisomes. 100% of fluorescence in all graphs is the initial fluorescence of phycobilisomes without quenching. Error bars: standard deviation. Each curve represents the mean of three independent measurements.

Figure 8: Effect of the presence and position of a His-tag on OCP-PBS interaction. (A-C) *Synechocystis* (A, C) and *Planktothrix* (B) PBS fluorescence quenching induced at 23°C in 0.5 M phosphate buffer by native (non-tagged; black), N-tagged (red) and C- tagged (blue) CAN-functionalized *Synechocystis* (A) and *Planktothrix* (B, C) OCPs. The OCP was pre-photoactivated by illumination of strong white light (5 000 μmol photons m^{-2}. s^{-1}) at 4°C. The ratio OCP:PBS was 40:1. (D-F) Dark recovery of fluorescence in *Synechocystis* (D, F) and *Planktothrix* (E) PBS. 100 % of fluorescence in all graphs is the initial fluorescence of phycobilisomes without quenching. Error bars: standard deviation. Each curve represents the mean of three independent measurements.

Figure 9. The naturally occurring OCP dimer is found in all OCP crystals, including those of Plankto-OCP. Residues involved in the dimerization are highlighted in yellow, whereas residues involved in the formation of interface X are highlighted in purple. Dark and light colouring indicate residues involved in polar and van der Walls interactions, respectively. Squares highlight residues present in alternate conformations in at least 50% of the analyzed Plankto-OCP chains. (A) The secondary structure of OCP is overall well conserved amongst Plankto-OCP structures obtained in different space groups and with different pigments. White dots highlight residues which are observed in alternate conformations. Blue stars indicate residues which have been shown to play a role in the OCP-PBS interaction, and red stars point to residues that could be at the origin of the stronger attachment of Plankto-OCP to the Syn-PBS. (B-C). The asymmetric unit of the *P*2$_1$ crystals features a dimer (here shown as a ribbon with the two facing monomers colored sequence-wise, from cold (N-ter) to hot (C-ter) colors), whereas in *C*2 crystals, the dimer is crystallographic, hence only a single monomer is found in the asymmetric unit. (D) Polar contacts at the dimerization interface involve a conserved salt-bridge between D19 and R27, as well as conserved H-bonds between facing D6 and T90, and

between facing N134 and N14, T15, and T17. (E, F, G) The *C*2 structures display a more compact conformation than the *P*2₁ structures, at both the dimer (E, F) and at the monomer levels (G). The figure illustrates the trajectory followed by Plankto-OCP as we interpolate from the *C*2-CAN to the *P*2₁-CAN structure, highlighting the secondary structure elements which diverge most upon packing in the two crystal types. Arrows show the overall direction travelled by domains as we interpolate between the *C*2-Can and *P*2₁-CAN Plankto-OCP.

Figure 10: The *Planktothrix* OCP features two similarly large packing interfaces in crystals. In Plankto-OCP crystals, a large interface, additional to the dimerization interface (Table S1), is found which we coined interface X (Table S3). This interface, mainly contributed by by helices αD, αG and αJ and by the αC-β4 and β5-β6 loops, matches the dimerization interface, in *P*2₁ crystals (BSA of ~1050 Å^2), but largely exceeds it, in the *C*2 crystals (BSA of ~1600 Å^2). Changes in the extent of interface X result in a reorientation of domains in each monomer forming the naturally-occurring dimer, and in an increase in the opening angle between monomers, in the dimer. Arrows indicate the direction and distance along which Cα atoms travel as we interpolate from the *P*2₁ to the *C*2 crystals.

Figure 11: Plankto-OCP structures differ in the compaction of the monomer as well as in the internal structure of the NTD. (A) The *C*2 (orange), and *P*2₁ chain A (slate) and chain B (grey) are overlaid as ribbons. Structural alignment, performed using the CTD atoms, highlight the change in opening angle between the CTD and the NTD. Indeed, the CTD structure is highly conserved with hardly no conformational changes observed amongst structures. Large differences are yet seen in the NTD, notably in the αC-αD and αG-αH loops, but as well in the relative positioning of αC and αD helices. Here, the Plankto-OCP-CAN structures are shown, but the same observations were made when comparing the Plankto-OCP-ECN structures. (B) Close up view on CAN and on the residues lining the carotenoid tunnel. A change in the orientation of the carotenoid is seen upon compaction of the OCP structure due to change in space group.

Figure 12: Conformational changes observed upon change of the functionalizing carotenoid are limited to the NTD. (A) The structure of Plankto-OCP-CAN is shown as a ribbon colored from cold to hot colors as a function of the RMSD to the Plankto-OCP-ECN structure. (B) Close-up view on the carotenoid and residues lining the homonymous tunnel. The orientation in (B) is similar to that in the upper panel of (A).

Figure 13: Crystal packing traps different conformations of the Ntag-Plankto-OCP monomers. (A) Changes in Cα-Cα distances across in the various ECN- and CAN-functionalized *C*2 and *P*2₁ chains were monitored by computing Cα-Cα difference-distance matrices (DDM). As a reference structure, we used the *C*2 Plankto-OCP-CAN (2 first rows), or either chain A or C of the *P*2₁ PlanktoOCP-CAN structure (third line). In each DDM, the lower and upper panels (separated by a sketch of the secondary structure) show the changes in Cα-Cα distances for alternate conformers A and B with respect to the reference structure. Indeed, alternate conformations are seen in all Plankto-OCP structures. The overall similarity between upper and lower panels indicates that alternate conformations hardly affect the protein backbone. In the *P*2₁ crystals, two chains are found, which either display a more expanded (chain A) or a more compact (chain B) structure, due to changes in the opening angle between the NTD and the CTD. The DDM further indicates that these changes stem from helix αD, and the αC-αD and αG-αH loops, either drawing away (chain A) or coming closer (chain B) to the

CTD, respectively. Comparison of the *C*2-CAN and *C*2-ECN structures suggests that the presence of CAN results in a more compact protein. Support to this hypothesis could not be obtained from comparison of the *P*2$_1$ chain A or *P*2$_1$ chain B structures. Nonetheless, we observe a similar trend when comparing, either in the CAN-functionalized or the ECN-functionalized states, *P*2$_1$ chain C and *P*2$_1$ chain A. Thus, changes in functionalizing carotenoid have a lesser influence on the OCP conformation than changes in space group. (B) DDM calculated for the isolated NTD of Syn-OCP-CAN vs. Syn-OCP-CAN. This DDM suggests that upon photoactivation, large scale conformational changes occur in the NTD that mainly result in helix αB drawing away from helices αD to αG, while the αC-αD loop comes closer to these and to αH to αI. Also, αG edges closer to helices αH to αI, while the αG-αH loop draws farther. (C) DDM calculated for Syn-OCP$_{CAN}$ vs. Syn-OCP$_{ECN}$. Hardly no change in the Syn-OCP structure is seen upon change in the functionalizing carotenoid.

Tables:

Table 1: Lifetime, time constants and quantum yields obtained from femtosecond and nanosecond transient absorption experiments. (A) Lifetimes of ICT/S$_1$/S*/P$_1$ states derived from femtosecond transient absorption measurements (from data in Figure 5 and Figure S2), and estimated formation quantum yields derived from preexponential factors at 490 nm (the magnitude of the bleaching band of each DAS was extracted from the fitting procedure; for more details, see the Materials and Methods section and Nizinski et al., submitted; doi.org/10.1101/2021.12.26.474187). The standard error is 10%. P$_1$ yields are corrected for its positive absorbance contribution at 500 nm. (B) Time constants and yields (percentages in brackets) derived from ns-s transient absorption measurements for P$_1$, P$_2$/P$_2'$ and P$_3$/P$_{N-M-X}$. Only in the case of P$_1$ are the value in brackets actual quantum yields; for P$_2$/P$_2'$ and P$_3$/P$_{N-M-X}$, they rather indicate the relative contribution of the corresponding exponential terms to the overall decay and growing components (indicated in bold). Percentages in the OCP^R column are formation quantum yields of the red absorbing intermediates remaining at 10 ms (determined by a comparative actinometry method with ruthenium complex; for details, see Material and Methods section and [45]).

Table 2. Data collection and refinement statistics. Statistics for the highest-resolution shell are shown in parentheses.